JES Collection of Invited Battery Review Papers

Review—Electromobility: Batteries or Fuel Cells?

Oliver Gröger,[a] Hubert A. Gasteiger,[b,*,z] and Jens-Peter Suchsland[c]

[a] *Volkswagen AG, 38436 Wolfsburg, Germany*
[b] *Chair of Technical Electrochemistry, Technische Universität München, 85748 Garching, Germany*
[c] *SolviCore GmbH & Co. KG, 63457 Hanau, Germany*

This study provides an analysis of the technological barriers for all-electric vehicles, either based on batteries (BEVs) or on H_2-powered proton exchange membrane (PEM) fuel cells (FCEVs). After an initial comparison of the two technologies, we examine the likely limits for lithium ion batteries for BEV applications, and compare the projected cell- and system-level energy densities with those which could be expected from lithium-air and lithium-sulfur batteries. Subsequently, we will review the current development status of H_2 PEM fuel cells, with particular attention to their viability with regards to the required amount of platinum and the resulting cost and availability constraints.

 [DOI: 10.1149/2.0211514jes]

Manuscript submitted September 1, 2015; revised manuscript received September 8, 2015. Published October 9, 2015. *This paper is part of the JES Collection of Invited Battery Review Papers.*

It is widely accepted that global warming is caused by CO_2 emissions and that they must be substantially reduced in order to prevent climate change. Since ≈23% of the world-wide CO_2 emissions are due to transportation, ≈75% of which are contributed by the road sector (numbers from 2012[1]), a reduction of CO_2 emissions from vehicles is imperative to combat global warming. Towards this goal, many countries have passed legislature to lower passenger vehicle emissions over the long term like, e.g., the European Union mandate for 95 g_{CO2}/km fleet average emissions by 2020.[2] The analysis by Eberle et al.[3] in Figure 1 suggests that this rather ambitious goal can only be met by means of extended range electric vehicles or all-electric vehicles in combination with the integration of renewable energy (e.g., wind and solar). Without increased integration of renewable energy sources and basing the calculations on the current European electricity generation mix, the only vehicle concept which could meet the 95 g_{CO2}/km target are pure battery electric vehicles (BEV100 in Fig. 1). However, for electricity produced entirely by renewable energy sources, the 95 g_{CO2}/km target could also be met by extended range electric vehicles with 40 miles all-electric range (E-REV40 in Fig. 1), if 50% of driving is powered by the battery (i.e., the average driving range would have to be below 80 miles), or by fuel cell electric vehicles (FECVs), with hydrogen produced by water electrolysis. While these propulsion concepts look promising, their contribution to CO_2 emission savings in the transportation sector would only be meaningful if their market penetration were substantial. In the absence of government regulations, the latter largely hinges on consumer acceptance, which in turn strongly depends on cost. In addition, in the case of BEVs, recent studies clearly showed that BEV driving range (closely followed by cost) are the predominant variables determining consumer acceptance.[4]

In the following we will thus focus on the two vehicle types, which would be capable to meet and exceed the CO_2 emission targets of 95 g_{CO2}/km on the long-term, viz., pure BEVs and hydrogen powered FCEVs. For both vehicle types, but particularly for the latter, meaningful CO_2 emission reductions require the predominant use of renewable energy, which in turn necessitates the development and implementation of viable large-scale electricity storage and/or the generation/storage of hydrogen from renewables. A discussion of this important aspect is beyond the scope of this article, but the following references provide good overviews on large-scale electricity storage options (e.g., Refs. 5 and 6), on hydrogen generation by electrolysis or from biomass (e.g., Refs. 7 and 8), and on hydrogen storage (e.g., Ref. 3). Since vehicle cost and range largely control market penetration, we will first provide a rough estimate of the cost/range projected for BEVs and FCEVs. Next, we will briefly review the current status and the expected future progress in lithium ion battery (LiB) technology, which is currently used to power BEVs. This will be followed by an assessment of the perceived technological barriers and the potential energy density gains for so-called post-LiBs, namely lithium-oxygen and lithium-sulfur batteries. Last, we will discuss the materials development challenges for FCEVs, focusing on approaches to reduce platinum catalyst loadings and to improve fuel cell durability.

Cost and Range Estimates/Constraints for All-Electric Vehicles

The limitations imposed on both cost and driving range of BEVs may be illustrated by back-on-the-envelope calculations using the currently assumed energy density and cost constraints of lithium ion battery (LiB) systems. This requires an estimate of the average energy consumption per driven mile, which strongly depends on vehicle weight, the assumed drive-cycle, and the vehicle performance characteristics (maximum speed and acceleration). For example, the i3 BEV produced by BMW has an average energy consumption of ≈0.21 kWh_{net}/mile,[9] which lies in between the values cited for a mid-size car of ≈0.17 kWh_{net}/mile by Wagner et al.[10] or of ≈0.30 kWh_{net}/mile in a more recent study by Gallagher et al.[11] Using the value of 0.21 kWh_{net}/mile, the net energy required for 100 and 300 miles range equates to 21 and 63 kWh_{net}, respectively (see first line in Table I). Assuming a discharge efficiency of 95% (optimistic, but possible) and that 80% of the energy contained in the battery can be utilized (i.e., 80% state-of-charge window to prevent both battery overcharge which could pose a safety risk and complete discharge which would negatively affect durability),[10] the required name-plate energy of the battery-system for different driving ranges can be calculated (see second line in Table I). Using the highest projected value for the specific energy of advanced lithium ion battery-systems (≈0.20,[10] ≈0.23,[12] and ≈0.25 $kWh_{name\text{-}plate}/kg_{battery\text{-}system}$[11]), the battery-system weights for BEV ranges of 100 and 300 miles amount to 110 and 330 kg, respectively (see Table I). Here it should be noted that the gain in vehicle weight would be larger than the estimated battery weight increase due to the need for additional structural reinforcements and the effect of larger weight on energy consumption per mile.[3,10] Unfortunately, the current cost of battery-systems is not readily available, but is likely on the order of ≈250 $/$kWh_{name\text{-}plate}$, with long-term estimates for large-scale production of advanced LiB technologies (Si-based anodes and high-capacity cathodes) on the order of ≈125 $/$kWh_{name\text{-}plate}$.[11] The thus projected current battery-system costs shown in Table I illustrate why currently manufactured

*Electrochemical Society Fellow.
[z]E-mail: hubert.gasteiger@tum.de

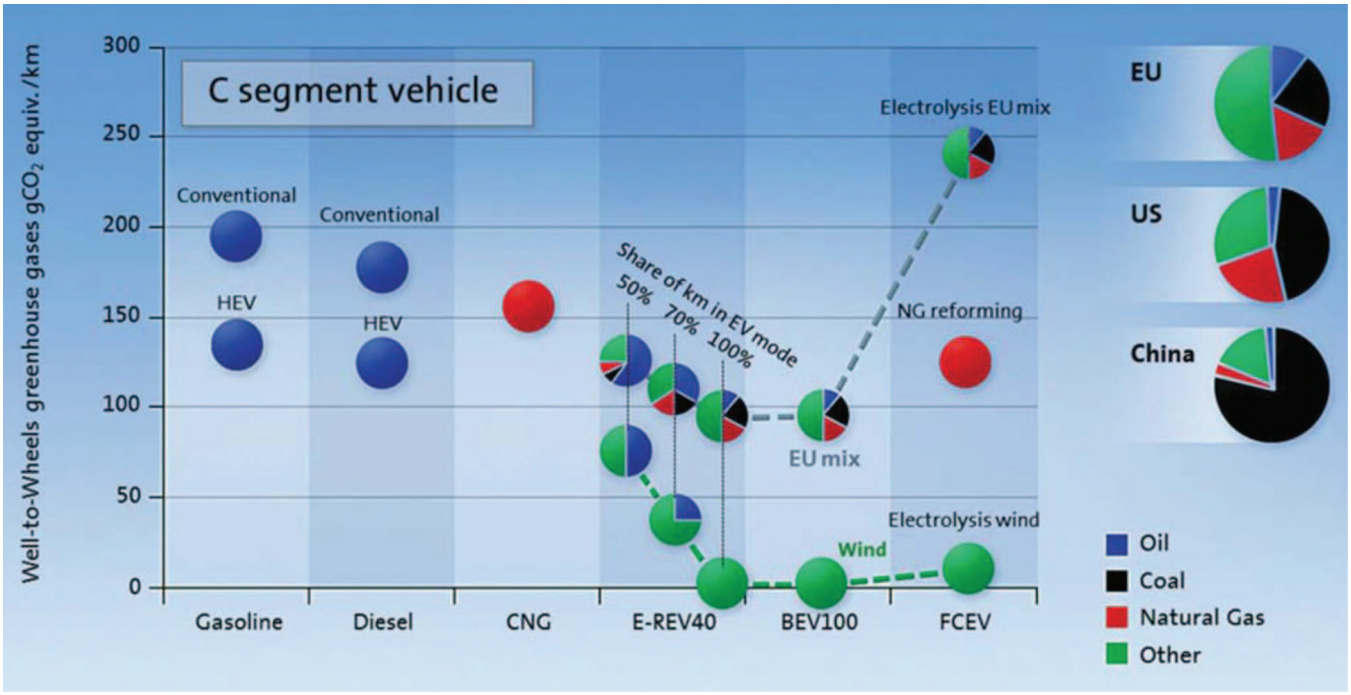

Figure 1. Well-to-wheel greenhouse gas emissions for C segment vehicles (≡ compact cars): i) conventional or hybridized (HEV) internal combustion vehicles operating with gasoline, diesel, or compressed natural gas (CNG); ii) extended range electric vehicles with 40 miles all-electric range (E-REV40) with various usage fractions in the all-BEV mode or full battery electric vehicle (BEV100), assuming the EU electricity production mix (upper symbols) or electricity entirely based on renewables (lower symbols); and, iii) fuel cell electric vehicle (FCEV), with hydrogen produced either by natural gas or by electrolysis using the EU electricity production mix (upper symbols) or electricity entirely based on renewables (lower symbols). (Reproduced from U. Eberle et al.[3] with permission from the Royal Society of Chemistry.)

Table I. Estimated required net energy and name-plate energy of the battery as well as battery-system weight and cost for BEVs (compact car) with a driving range of 100, 200, or 300 miles. Assumed were a specific energy of 0.25 $kWh_{name\text{-}plate}/kg_{battery\text{-}system}$, 95% discharge efficiency, battery operation with a 80% state-of-charge window, and an average energy requirement of 0.21 kWh_{net}/mile.

driving range	100 miles	200 miles	300 miles
required net energy [kWh_{net}]	≈21	≈42	≈63
required name-plate energy [$kWh_{name\text{-}plate}$]	≈28	≈56	≈84
battery-system weight [kg]	≈110	≈220	≈330
battery-system cost at 250 \$/$kWh_{name\text{-}plate}$ [k\$]	≈6.9	≈13	≈21
battery-system cost at 125 \$/$kWh_{name\text{-}plate}$ [k\$]	≈3.5	≈7.0	≈10

BEVs targeting the mid-size car market/pricing are limited in range to ≈100 miles (e.g., the BMW i3, the Mitsubishi i-MiEV, etc.) and why larger driving ranges can only be realized for the luxury or sports car market (e.g., the Tesla Model S). With the above long-term cost estimate, a 300 mile driving range may not be feasible for the mid-size car market/pricing due to excessive battery-system costs (see last row in Table I) even for very optimistic long-term battery-system cost assumptions. In summary, without radical changes in battery and/or vehicle technology, the production of BEVs with driving ranges of ≈200 miles might be challenging and for anywhere near 300 miles is likely not feasible for the mid-size car market due to battery weight and cost constraints.

Table II. Current and long-term cost projections for a 80 kW H_2-powered fuel cell system and for a 70 MPa H_2-tank system for 5 kg of H_2 to enable ≈300 miles FCEV range (assuming a production rate of 500,000 vehicles/year). Note that this does not include cost for a high-power propulsion battery (e.g., 1.8 kWh/35 kW in GM's HydroGen4[3]).

	projection of current cost [k\$]	projection of long-term cost [k\$]
fuel cell system	≈4.4	≈3.2
H_2-tank system	≈2.8	≈1.7
H_2 fuel cell + tank system	≈7.2	≈4.9

Contrary to BEVs, driving ranges of ≈300 miles under real-road conditions have already been demonstrated for hydrogen-powered FCEVs using ≈5 kg H_2 stored in high-pressure tanks (70 MPa H_2 tanks with ≈5.5%wt hydrogen; 1 kg H_2 providing a range of ≈63 miles[3]). Cost estimates, however, are probably even more uncertain for FCEVs than for BEVs, due to the very low production volumes (e.g., Toyota announced the production of 700 Mirai FCEVs in 2015). Estimates published by the US Department of Energy are based on production rates of 500,000 vehicles/year: ≈55 \$/kW for an 80 kW_{net} fuel cell system (≈40 \$/kW long-term)[13] and ≈560 \$/kg_{H2} for the tank system (≈333 \$/kg_{H2} long-term).[14] As shown in Table II, a H_2 fuel cell system including H_2 storage designed for ≈300 miles range may satisfy long-term cost requirements for a mid-size car market (right column in Table II) and will most likely be substantially cheaper than a battery-system for ≈300 miles range (compare right column of Table I with last row of Table II). On the other hand, for a ≈100 mile range, BEVs most likely will have a cost advantage. Analogously, as outlined by Wagner et al.,[10] a BEV battery-system is predicted to have a lower weight compared to a fuel cell plus H_2 tank system at ≈100 mile range, but will have a weight disadvantage for a ≈300 mile range. In summary, this simple and admittedly rather rough analysis suggests

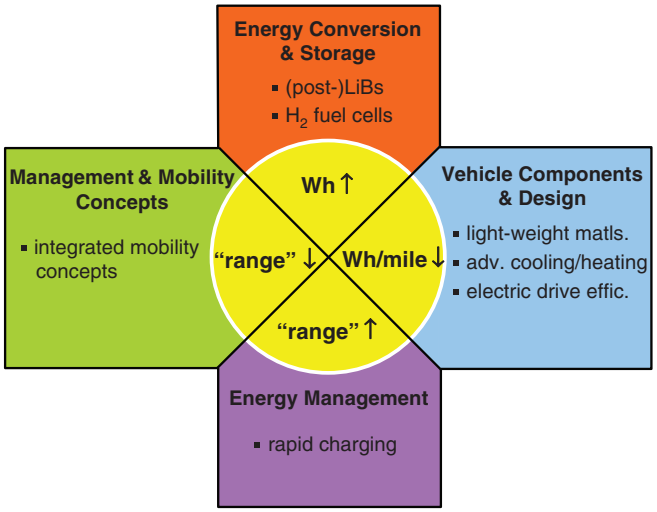

Figure 2. Factors influencing the needed/perceived range of all-electric vehicles: i) amount of storable energy (in units of Wh) either in (post-)lithium ion batteries or in hydrogen to power H_2-fuel cells; ii) vehicle energy consumption (in units of Wh/mile); iii) the customer's perceived range, strongly affected by the recharge rate; and, iv) novel integrated mobility concepts.

that BEVs will be the preferred option for short-range vehicles, while FCEVs are more suitable for large driving distances.

Since the societal value of electromobility requires substantial market penetration, it hinges on consumer acceptance of all-electric vehicles. As mentioned in the Introduction, the main obstacles to BEV consumer acceptance are driving range and cost.[4] The observed paradox with regards to driving range is the difference between actually *needed* and *preferred* driving range, which is related to several factors:[15] i) inaccurate understanding of needed driving range; ii) habitually large driving range of conventional vehicles; iii) so-called "range anxiety", i.e., the fear of getting stranded; and, iv) lack of experience with limited-range vehicles. Past studies have shown that the average or mean daily driving range underestimates the actual driving range need, which is better reflected by values of the longest daily driving distance per week or per year.[15] In this study, with roughly 70 German BEV drivers, it was found that the maximum daily driving range per week of ≈100 miles would be sufficient for 75% of the participants. On the other hand, while 75% of the drivers considered ≈100 miles as *minimum acceptable range*, ≈160 miles were considered an *appropriate range* by 75% of the drivers. Similarly, other studies report an average minimum range desired of ≈215 miles,[4] and a review of the literature in Reference 15 shows similar driving range values between 100 and 200 miles. While the increase of BEV use in the coming years will provide more accurate values for the *appropriate* BEV driving range, current studies suggest that 150–200 miles under real-life driving conditions might be required for wide-spread consumer acceptance.

Since driving range is a critical factor determining market penetration, it is useful to briefly examine the options to increase the actual or the *perceived* range of all-electric vehicles shown in Figure 2. Quite clearly, increasing the gravimetric and volumetric energy density by means of advanced LiBs and so-called post-LiBs would be the most straightforward way toward long-range BEVs; alternatively, H_2-powered FECVs would be another path toward long-range all-electric vehicles. Driving range could also be increased by reducing energy consumption per mile (see blue segment in Fig. 2), which can be accomplished by the use of light-weight materials (e.g., carbon composite chassis explored by BMW[9]), by improvements in electric-drive efficiency (e.g., Ref. 16), and by advanced vehicle climatization concepts (e.g., for the UDDS (urban dynamometer drive schedule) drive cycle, BEV driving range reductions by ≈17 and ≈50% have been reported for cooling and heating, respectively[17]).

In some studies it has been noted that the adequate BEV range *perceived* by the customer could be lower if the recharging time would be sufficiently short[4] (see purple segment in Fig. 2). Therefore, companies have been establishing fast-charging stations (ranging, e.g., from 24 kW by BMW[18] to 120 kW by Tesla[19]). For a 100 mile-range BEV requiring ≈21 kWh_{net} (see Table I), complete recharge could be accomplished within ≈60 min. using a 24 kW charging station and within ≈12 min. using a 120 kW charging station (assuming 90% charging efficiency). Thus, only with high-power 120 kW charging stations, recharging times close to the refilling time of conventional cars can be obtained for 100 mile range BEVs. For larger-range BEVs, recharging will be substantially longer and the business case for ≥120 kW charging stations is probably questionable[20] (note that recharging a 63 kWh battery for a 300 mile BEV within 5 minutes would require 0.76 MW electric power, which would likely result in rather unreasonable charging infrastructure cost for passenger vehicle use). On the other hand, FCEVs requiring ≈5 kg H_2 for 300 miles range can be refilled within conventional filling times (≈8 min. acc. to the 0.6 kg_{H2}/min. filling rate reported by DoE,[21] and only 3.5 min. from 20 to 95% fill-level for Toyota's Mirai vehicle[22]), so that they would have similar range and refilling attributes as conventional vehicles.

Finally, one might ask the question whether future mobility concepts and mobility expectations still require large driving distances (see green segment in Fig. 2). A new generation of drivers might not desire large-range vehicles, establishing convenient short-term car leasing concepts in cities might replace the desire for car ownership, and/or growing experience of drivers with BEVs might push the *perceived* driving range closer to the actually *needed* driving range (indications for this have been seen in recent studies[15,23]). For these reasons, the wide-spread adoption of BEVs might not only be a question of technology (battery, vehicle design, and charging infrastructure advancements), but also a question of changing customer expectations and desires.

In summary, the deciding factor whether BEVs or FCEVs will take the major share in the future passenger vehicle market is most likely the needed/perceived vehicle driving range, with BEVs more suitable for short driving ranges and FCEVs for large driving ranges and/or large vehicles. In either case, however, cost and durability challenges still remain and at least evolutionary technology advances are still required.

Lithium Ion Battery Status and Expected Advances

In the following, we will examine the status and the expected advances in specific energy and volumetric energy density of lithium ion battery-systems. Figure 3, published by Gallagher et al.[11] summarizes these values for different lithium ion battery technologies, showing that the useable energy in current BEVs ranges from ≈0.07 $kWh_{use}/kg_{battery\text{-}system}$ for the Nissan Leaf to ≈0.12 $kWh_{use}/kg_{battery\text{-}system}$ for the Tesla Model S (see white bubble in Fig. 3). It should be noted that in terms of installed battery energy (name-plate energy), this would correspond to ≈0.10 and ≈0.15 $kWh_{name\text{-}plate}/kg_{battery\text{-}system}$, respectively, since the useable system energy of 100 kWh_{use} in Figure 3 was based on an installed name-plate battery energy of 128 $kWh_{name\text{-}plate}$ (i.e., the product of state-of-charge-window and discharge efficiency equals 0.78 (see Excel file provided as supporting information of Reference[11]), essentially identical to the value of 0.76 used in Table I). A similar value of ≈0.09 $kWh_{name\text{-}plate}/kg_{battery\text{-}system}$, was reported for BMW's i3 BEV.[12] Figure 3 also projects the specific energy for the graphite/NMC111 ($LiNi_{0.33}Mn_{0.33}Co_{0.33}O_2$ sometimes also referred to as NMC333) active material set (purple bubble in Fig. 3) which by now is sufficiently mature for use in vehicles and amounts to ≈0.15 ± 0.02 $kWh_{use}/kg_{battery\text{-}system}$ (or ≈0.19 ± 0.03 $kWh_{name\text{-}plate}/kg_{battery\text{-}system}$), thus being already quite close to the value of 0.25 $kWh_{name\text{-}plate}/kg_{battery\text{-}system}$ used as the basis for the estimates in Table I.

Replacing graphite anodes with silicon/carbon-composites and the layered-oxide NMC111 cathode material with "layered-layered" $xLi_2MnO_3 \cdot (1\text{-}x)LiMO_2$ (M being a mixture of Ni, Co, and Mn),[24]

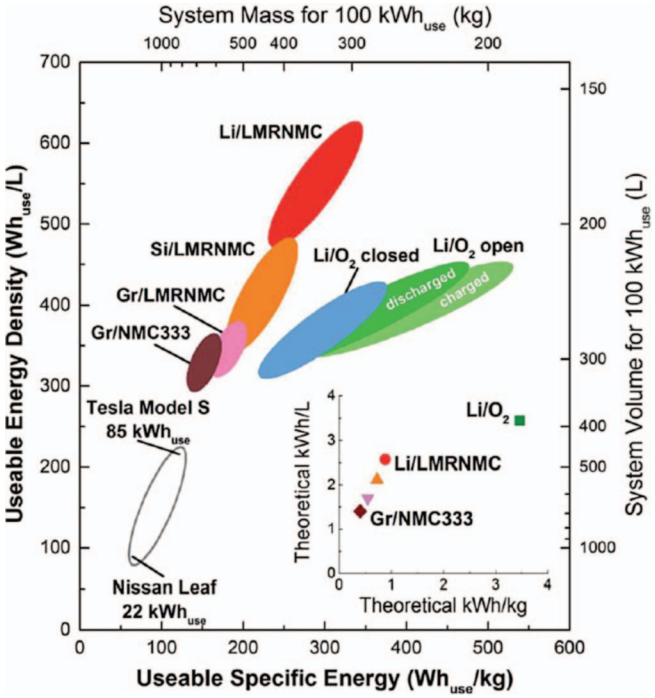

Figure 3. Projected system-level useable gravimetric (Wh_{use}/kg) and volumetric (Wh_{use}/L) energy for different lithium ion battery systems with 100 kWh useable energy and 80 kW net power. Note that this system corresponds to a name-plate battery energy of 128 kWh, i.e., the product of state-of-charge-window and discharge efficiency needed to convert Wh_{net} (useable energy) into $Wh_{name\text{-}plate}$ (installed name-plate battery energy) is 0.78 (essentially identical to the value of 0.76 used in Table I); therefore, $Wh_{name\text{-}plate}/kg_{battery\text{-}system} = 1.28 \cdot Wh_{use}/kg_{battery\text{-}system}$. The inset shows the theoretical energy densities of anode/cathode active material combinations, i.e., without any other cell components. (Reproduced from K. G. Gallagher et al.[11] with permission from the Royal Society of Chemistry.)

referred to as Si/LMRNMC in Fig. 3 (see orange bubble), specific energies of ≈0.22 ± 0.04 $kWh_{use}/kg_{battery\text{-}system}$ (or ≈0.28 ± 0.05 $kWh_{name\text{-}plate}/kg_{battery\text{-}system}$) are projected. Unfortunately, the cycle-life of $xLi_2MnO_3 \cdot (1\text{-}x)LiMO_2$ cathodes (often also referred to as high-energy NMC or HE-NMC) is at best ≈100 cycles at 20% capacity loss (see, e.g., Ref. 25) and thus still insufficient for applications, so that currently no active material set would be able to reach the 0.25 $kWh_{name\text{-}plate}/kg_{battery\text{-}system}$ used in the projections of Table I. Consistent with the projections in Fig. 3, a recent very detailed survey and analysis by Andre et al.[12] concluded that in combination with a silicon/carbon-composite anode, the only cathode materials which could reach 0.25 $kWh_{name\text{-}plate}/kg_{battery\text{-}system}$ are HE-NMC, nickel-rich NMC811 ($LiNi_{0.8}Mn_{0.1}Co_{0.1}O_2$), and NCA ($LiNi_{0.8}Co_{0.15}Al_{0.05}O_2$) and that these materials could also satisfy the required volumetric energy density (an equally important value for the design of BEVs). Again, cycle life was found to be insufficient for any of these materials. In addition, at the higher positive potentials required for example for HE-NMC (≈4.7 V vs. Li/Li^+[25]), the stability of the aluminum current collector[26] as well as of the conductive carbon additive and the electrolyte[27] are compromised and may limit battery life. Albeit at a much lower level of maturity, other potential high-energy cathodes would be materials based either on the intercalation of two lithium ions per unit cell (e.g., Li_2MnSiO_4) or conversion materials (e.g., FeF_3).[12]

Based on HE-NMC, nickel-rich NMC, and/or NCA, the only option to significantly exceed 0.25 $kWh_{name\text{-}plate}/kg_{battery\text{-}system}$ would be their combination with metallic lithium anodes (see red bubble in Fig. 3), resulting in specific energy projections of ≈0.36 ± 0.06 $kWh_{name\text{-}plate}/kg_{battery\text{-}system}$. Unfortunately, many decades of research still have not been able to resolve the issues of shape-change, dendrite formation, and poor Coulombic efficiency (due to continuous electrolyte consumption caused by an unstable SEI) of metallic lithium anodes (lithium metal foils or lithium metal powders) in combination with liquid electrolytes,[28,29] so that it remains unclear whether stable long-term cycling with metallic lithium anodes could ever be achieved (the only exception are liquid solvent free lithium-polymer batteries, in which the polymer conductivity limits battery operation to temperatures above ≈60°C).

In summary, despite the long research history in the lithium ion battery field and the large active research community, specific energies of lithium ion batteries significantly larger than 0.25 $kWh_{name\text{-}plate}/kg_{battery\text{-}system}$ are not yet on the horizon. Therefore, based on the arguments made in the previous Section with regards to cost and range estimates/constraints for all-electric vehicles, lithium ion battery based BEVs with 200 miles range or more will probably be out of scope for the mid-size car market/pricing. Therefore, much of the recent attention has focused on so-called post-lithium ion batteries like lithium-oxygen and lithium-sulfur batteries, which will be reviewed in the next Section.

Lithium-Oxygen Battery – Energy Density Projections and Challenges

The observed discharge product in the lithium-oxygen battery is Li_2O_2,[30] i.e., the overall cathode discharge reaction is $2\,Li^+ + 2\,e^- + O_2 \rightarrow Li_2O_2$. During the first phase of excitement, the energy density of lithium-oxygen batteries was often paralleled with the energy density one would calculate for metallic lithium using the reversible potential for Li_2O_2 of 2.96 V, which yielded the breath-taking value of ≈11.4 kWh/kg_{Li}. This is of course misleading, since the oxygen content in the Li_2O_2 discharge product is quite large and needs to be included in the specific energy calculation, yielding a still very high value of ≈3.5 kWh/kg_{Li2O2} (this is shown in the inset of Fig. 3). For a fair comparison with lithium ion battery electrodes, the weight of the electrodes (i.e., conductive carbon and binder) needs to be included and the actually observed discharge potential (≈2.75 V) instead of the reversible potential should be used,[31] as is done in Table III, which provides an estimate of the gravimetric energy density of advanced lithium ion battery cathodes in comparison with that of a Li-O_2 battery cathode forming Li_2O_2 discharge product. As shown in Table III, the difference in $kWh/kg_{electrode}$ is ≈3-fold, which suggests a big advantage of Li-O_2 batteries compared to lithium ion batteries

Table III. Estimated maximum gravimetric energy density of cathode electrodes (dry basis, i.e., without electrolyte) for an advanced lithium ion battery HE-NMC cathode as well as for Li-O_2 battery cathodes, for which complete pore filling with either Li_2O_2 or Li_2O discharge product is assumed. The Li-O_2 battery cathode estimates are based on volume fractions of $\varepsilon_{carbon+binder} = 0.15$, $\varepsilon_{electrolyte} = 0.25$, and $\varepsilon_{Li2Ox} = 0.60$, which may be compared to typical carbon volume fractions of carbon fiber papers of $\varepsilon_{carbon} = 0.15$–$0.25$ and of carbon-black based electrodes of $\varepsilon_{carbon} \approx 0.15$ (for more details see Ref. 31). Also, for comparison, the typical electrolyte volume fraction in lithium ion batteries is $\varepsilon_{electrolyte} \approx 0.35$.

HE-NMC	Li_2O_2 discharge product	Li_2O discharge product
≈90%wt HE-NMC	≈80%wt Li_2O_2	≈77%wt Li_2O
≈10%wt carbon+binder	≈20%wt carbon+binder	≈23%wt carbon+binder
≈260 $mAh/g_{electrode}$	≈900 $mAh/g_{electrode}$	≈1350 $mAh/g_{electrode}$
≈3.5 $V_{average}$ (vs. Li-anode)	≈2.75 $V_{average}$ (vs. Li-anode)	≈2.75 $V_{average}$ (vs. Li-anode)
≈0.82 $kWh/kg_{electrode}$	≈2.5 $kWh/kg_{electrode}$	≈3.7 $kWh/kg_{electrode}$

(conceptionally, as shown in Table III, a ≈4.5-fold gain would be obtained if it were possible to selectively catalyze the formation of Li_2O discharge product, which thermodynamically is equally possible,[31] but which has not yet been observed[30]).

Unfortunately, the recent battery-system analysis by Gallagher et al.[11] (see Fig. 3) revealed that the higher complexity of Li-O_2 compared to lithium ion batteries leads to substantially lower energy densities in the final battery-system, so that the above ≈3-fold specific energy advantage on the basis of the cathode electrode diminishes to at best a factor of ≈1.5–2 on the system-level if compared to a an advanced lithium ion battery system, viz., Si/HE-NMC (see blue/green bubbles vs. orange bubble in Fig. 3). At the same time, however, if one were to assume that one were able to design a durable lithium metal anode for a Li-O_2 battery, one would expect to be able to do the same for a lithium ion battery, in which case the gain in specific energy of the battery-system would be less than a factor of ≈1.5 (see blue/green bubbles vs. red bubble in Fig. 3). In summary, the specific energy of Li-O_2 battery-systems would most probably not exceed that of advanced lithium ion batteries by more than a factor of ≈1.5. In terms of volumetric system-level energy density, Li-O_2 batteries quite definitely would be inferior to lithium ion batteries.

Despite this rather sobering outcome of the above system-level analysis, even a factor of ≈1.5 in specific energy could make a meaningful difference to the achievable range of BEVs, so that it is worthwhile to briefly review the current understanding of the Li-O_2 battery chemistry (for a very detailed review see Reference 30). The first Li-O_2 battery discharge in alkyl carbonate electrolytes (i.e., in conventionally used LiB electrolytes) was discovered 1996 by Abraham and Jiang,[32] and in 2008 Débart et al.[33] demonstrated rechargeability over ten cycles, which triggered many further studies. It was not until 2010, however, that Mizuno et al.[34] showed by TEM measurements that Li_2CO_3 and lithium alkyl carbonates were the predominant discharge product, despite the fact that they could demonstrate 100 cycles. Later on it was shown that alkyl carbonates react with the oxygen discharge products in an irreversible reaction and that all Li-O_2 experiments in alkyl carbonates constituted the consumption of electrolyte rather than a reversible reaction.[35] This was confirmed at the same time by McCloskey et al.,[36] who in addition to XRD and Raman spectroscopy also, for the first time, employed on-line mass spectrometry and on-line pressure measurements to demonstrate that the discharge reaction in alkyl carbonate electrolytes yielded e^-/O_2-values ≫ 2, while a value of 2 expected for the formation of Li_2O_2 from O_2 was obtained in DME (dimethoxy ethane) based electrolyte. Furthermore, while mostly CO_2 was observed during charge in alkyl carbonates, only O_2 was observed for DME based electrolyte.

The initial misinterpretation of the Li-O_2 charge/discharge data in alkyl carbonates by the research community illustrates that solely studying charge/discharge performance, particularly in small-scale test cells with large excess of electrolyte compared to commercial battery cells (≈100-fold higher electrolyte/electrode weight ratio), is not sufficient to demonstrate reversibility. Instead, these measurements must be accompanied by quantification of the number of e^-/O_2 during discharge and charge (expected to be 2) and by the quantification of the oxygen recovery over a charge/discharge cycle, which is analogous to the Coulombic efficiency commonly evaluated in lithium ion battery studies. Unfortunately, the reactivity of oxygen superoxide radicals (O_2^-) and/or adsorbed/solvated lithium superoxide (LiO_2) intermediates (see Fig. 4a) as well as Li_2O_2 is very high and they react with most of the investigated electrolytes, as was demonstrated later on by on-line mass spectrometry by several groups[37,38] (see, e.g., O_2-recovery and number of e^-/O_2 during charge in diglyme based electrolyte shown in Fig. 4b) Subsequently, the stability of binders and of electrolyte solvents was studied ex-situ by the reaction with potassium superoxide[39,40] and in studies which also include stability measurements by cyclic voltammetry and DFT calculations.[41,42] While the glymes are relatively stable against superoxide attack, they are prone to autooxidation[42] leading to degradation products (mostly formates and acetates) even after the first discharge, as detected by solution NMR.[40] So far, DMA (dimethyl acetamide) with $LiNO_3$ additive has shown the most promising stability,[43] even though 100% O_2-recovery has not yet been demonstrated neither for DMA nor for any other electrolyte solvent tested so far. A recent study suggests that a modified glyme (2,3-dimethyl-2,3-dimethoxybutane) might be a stable Li-O_2 electrolyte solvent, but while on-line mass spectrometry shows oxygen evolution during charge, the O_2-recovery is still substantially below 100%.[44] Similarly, the ionic liquid Pyr_{14}TFSI (1-butyl-1-methylpyrrolidinium bis(trifluoromethanesulfonyl)imide) was suggested to be stable in Li-O_2 cells,[45] but ex-situ tests have shown that it undergoes a Hofmann β-H elimination reaction in the Li-O_2 cell environment.[46] Thus, to the best of our knowledge, 100% O_2-recovery has not yet been demonstrated for any of the investigated electrolytes, so that the search for a stable electrolyte is probably the most critical challenge and need for the progress of Li-O_2 batteries.

In addition to the instability of the electrolyte in the Li-O_2 battery, the conductive carbon in the electrode reacts during both discharge and charge,[47,48,49] forming Li_2CO_3, which can only be oxidized at high potentials (>4 V), releasing CO_2 but not releasing any O_2 (as would be expected from $Li_2CO_3 \rightarrow CO_2 + 2\,Li^+ + 2\,e^- + 0.5\,O_2$), so that the oxidative decomposition of Li_2CO_3 must also result in electrolyte oxidation.[50] For this reason, alternative supports with higher

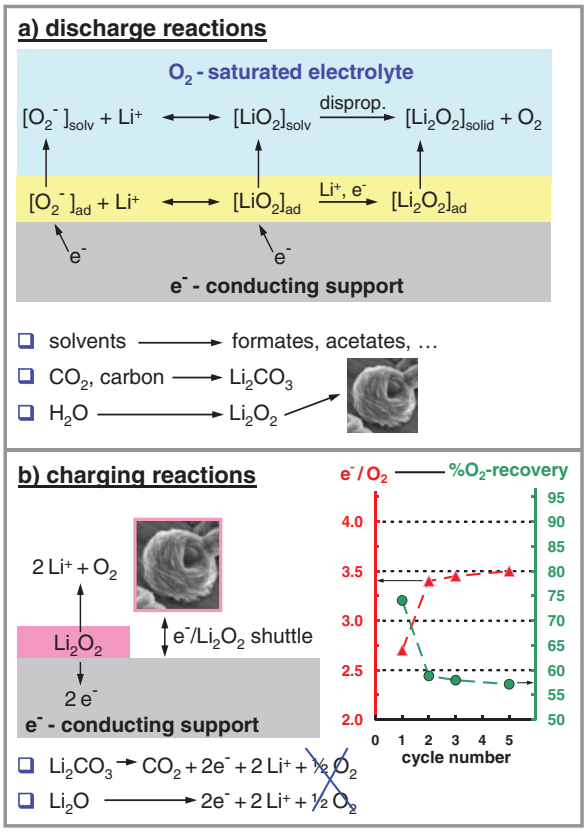

Figure 4. Reactions and experimental observations during discharge and charge of Li-O_2 cathodes. **a) Discharge reactions:** formation of adsorbed lithium superoxide, $[LiO_2]_{ad}$, which can either get solvated, $[LiO_2]_{solv}$ and disproportionate in the solution to solid lithium peroxide, $[Li_2O_2]_{solid}$ (≡ $2e^-/O_2$), or can get further reduced to adsorbed Li_2O_2, $[Li_2O_2]_{ad}$ (≡ $2e^-/O_2$); superoxide radical may also get partially solvated in the solution, $[O_2^-]_{solv}$. Furthermore, carbon and gas-phase CO_2 are found to react to lithium carbonate, Li_2CO_3, while water leads to the formation of large Li_2O_2 crystals (often referred to as toroids). **b) Charging reactions:** direct oxidation of thin Li_2O_2 surface films (pink area) corresponding to $2e^-/O_2$ and oxidation of large Li_2O_2 crystals by either an electron shuttle (redox shuttle) and/or the impurity facilitated solvation of Li_2O_2. The inset shows the number of e^-/O_2 and the %O_2-recovery (i.e., the oxygen round-trip efficiency) during the first charging cycles in diglyme based electrolyte from Ref. [38]; the lower-most reactions indicate that no O_2 is recovered during the charging of Li_2CO_3 and Li_2O, as was shown in Ref. 50.

oxidative stability like titaniuim carbide were examined, and promising charge/discharge cycle stability was reported for DMSO based electrolytes;[51] unfortunately, so far, these experiments could not be reproduced by other researchers.[30] In general, the reproducibility of Li-O_2 battery charge/discharge capacities and cycle-life is very poor, which at least partially is related to the strong sensitivity toward electrolyte impurities[40] and water[52] (here it should be noted that early Li-O_2 battery cell designs frequently used polymer tubing which is quite permeable to water vapor). Particularly the latter strongly enhances discharge capacities[52] and controls the morphology of the Li_2O_2 discharge product, which either deposits as nanometer-thin surface films resulting in low capacity[53,54] or as large crystallites in the electrode pore space yielding large capacities.[55,56]

In summary, no stable electrode components and electrolytes which would result in a demonstrated/reproducible 100% O_2-recovery over a Li-O_2 battery charge/discharge cycle have yet been confirmed. Therefore, further fundamental research and materials development is required to determine the viability of Li-O_2 batteries. If successful, the expected gains in specific energy of a battery-system would likely be not better than ≈1.5 –fold compared to advanced lithium ion batteries (Si/C-composite anodes with HE-NMC, NMC811, or NCA cathodes). In terms of electrocatalysis, little if any effect has been observed during discharge in electrolytes other than alkyl carbonates,[57] but redox-shuttles have been shown to accelerate the charging reaction.[58]

Lithium-Sulfur Battery – Energy Density Projections and Challenges

Lithium-sulfur battery concepts.— Due to the high specific energy of the sulfur cathode (1660 mAh/g_S), lithium-sulfur batteries have also been considered as promising post-LiB technology with substantial gravimetric energy density and cost advantages over LiBs. Figure 5 is a schematic depiction of the phenomena occurring in a lithium-sulfur battery during battery discharging. The so far low cycle-stability of lithium-sulfur batteries is largely caused by the formation of highly soluble polysulfides which diffuse/migrate to the anode. On the anode, long-chain polysulfides (Li_2S_x, with $x \geq 4$) can be further reduced to shorter-chain polysulfides (Li_2S_x, with $x = 3–6$) which enables a redox-shuttle process between the two electrodes and results in reduced Coulombic efficiencies. In addition, solid Li_2S_2 species and Li_2S can be formed on the anode from cross-diffusing polysulfides and, thus, can no longer take part in subsequent charge/discharge cycles, leading to a loss of cell capacity and severe cell degradation.

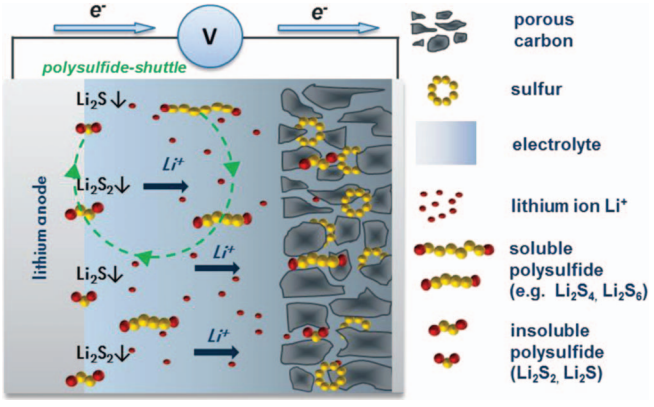

Figure 5. Illustration of the processes in a lithium-sulfur battery during discharge. Long chain polysulfides are primarily formed within the conversion reaction: lithium ions migrate to the cathode where long chained polysulfides (Li_2S_x, with $x = 3–6$) are formed. A part of these polysulfides diffuse to the anode where they are reduced to short chain polysulfides (Li_2S_x, with $x = 1–2$) (→ polysulfide shuttle mechanism). The newly formed short chain polysulfides are insoluble and precipitate on the surface of the anode or remain in the electrolyte. Since the sulfur content of the cathode consecutively depletes, this process is the main reason for a steady increase of capacity loss.

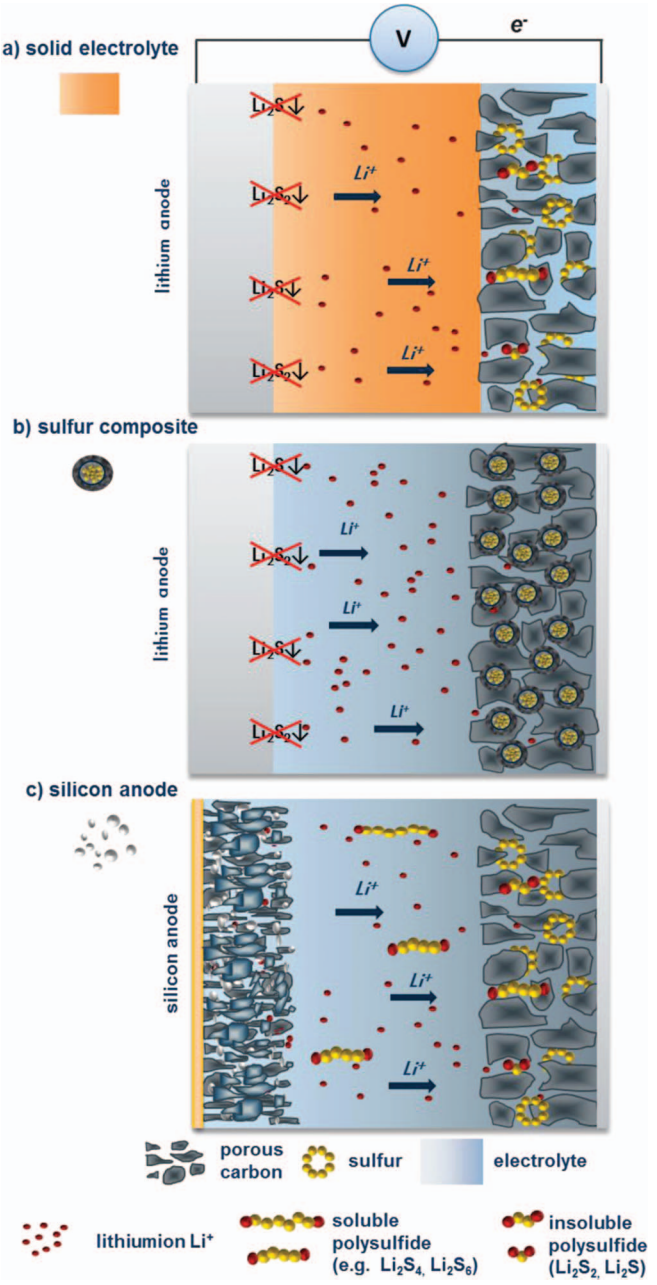

Figure 6. Different lithium-sulfur battery configurations to address the currently limited cycle-life with ether based electrolytes and with metallic lithium anodes: a) use of solid electrolyte, serving as polysulfide barrier; b) encapsulated sulfur particles; and, c) silicon anode.

To improve the cycle stability of lithium sulfur cells, three possible strategies can be evaluated. The first strategy involves the use of a lithium-ion-conducting solid electrolyte (Fig. 6a), which serves as a polysulfide diffusion barrier, thereby eliminating the polysulfide redox-shuttle and preventing the loss of sulfur from Li_2S precipitation on the anode. One example for a possible lithium-ion-conducting solid electrolyte is the P_2S_5-Li_2S system discussed by Agostini et al.[59] and by Nagao et al.[60] Also, as shown by Zhao et al.,[61] polymer-based systems can be used. However, one of the main challenges in the development of solid/polymer electrolytes is to achieve sufficiently high ionic conductivity at low temperatures. The second strategy (see Fig. 6b) is to develop novel cathode architecture concepts which suppress polysulfide mobility by, for example, embedding the sulfur into mesoporous structures or into porous carbon spheres.[62–65] The third

Table IV. Specifications of the pouch cell format/design and the cell components used for cell-level gravimetric and volumetric energy density projections.

pouch cell length/width/thickness	300/100/10 mm
pouch cell foil thickness	150 μm
anode Cu current collector thickness	10 μm
cathode Al current collector thickness	15 μm
separator thickness	25 μm
Separator porosity	55%

strategy is to use silicon based anodes instead of metallic lithium anodes (see Fig. 6c), with the hope that a more stable SEI on silicon compared to metallic lithium might prevent/suppress several detrimental processes: i) the polysulfide redox-shuttle; ii) the continuous consumption of sulfur via polysulfide reduction and Li_2S precipitation at the anode; and, iii) the long-term consumption of SEI stabilizing additives like $LiNO_3$,[66] whereby many additives which are effective for silicon anodes (e.g., vinylene carbonate[67] are not compatible with the ether based electrolytes commonly used in lithium-sulfur batteries. Another possible anode alternative might be tin-based electrodes as shown by Scrosati *at al*.[68]

Cell-level based lithium-sulfur battery energy density projections.— In the discussion of the lithium-oxygen battery (Lithium-oxygen battery – energy density projections and challenges section), it became clear that a simple comparison of the energy densities on the basis of the cathode active material-level can lead to overly optimistic projections of cell-level or system-level energy densities. While careful and rigorous cell- and systems-level energy density projections were presented for the lithium-sulfur battery system based on metallic lithium anode,[69,70] to the best of our knowledge, no comprehensive comparison has yet been published on the cell-level energy densities of lithium ion batteries versus lithium-sulfur batteries with either graphite or silicon anodes. In the following, we will therefore provide projected cell-level gravimetric and volumetric energy densities for lithium-sulfur batteries and compare them to LiBs with NMC111 cathodes and graphite, silicon, or metallic lithium anodes. For this, we use a common pouch cell format and commonly used current collector and separator materials, the specifications of which are listed in Table IV. The following projections clearly represents a best-case scenario, since the calculations are based on an anode/cathode capacity ratio of 1/1 and on the minimum amount of electrolyte which is that required to fill the pore volume of the electrodes and the separator (current lithium-sulfur batteries use much larger electrolyte volumes due to the continuous electrolyte consumption on the lithium metal anode).

The electrode specifications used in our cell-level energy density projections are listed in Table V (cathodes) and Table VI (anodes), whereby the electrode composition, the electrode porosity, and the average cell voltages are obtained from real cells in the case of graphite/NMC111 and are based on experimental cells for all other active material combinations. In order to facilitate a more straightforward comparison with lithiated LiB cathodes, Li_2S was chosen as cathode material for lithium-sulfur cells in these calculations (note that 68 %wt Li_2S correspond to 60 %wt S, which represents the highest sulfur content discussed in publications so far). For the lithium metal anode, a 2-fold lithium excess was assumed (i.e., anode/cathode capacity ratio of 2/1).

Based on the specifications listed in Tables IV–VI, we calculated the gravimetric and volumetric cell-level energy densities as a function of the areal capacity (in $mAh/cm^2_{electrode}$), which are shown in Figures 7 and 8. For the graphite/NMC111 cell ("C/NMC" in Figs. 7–9), the projected specific energy at the currently typically used areal capacity of ≈2.0 mAh/cm^2 is ≈0.21 kWh/kg_{cell} (see Fig. 7) and the volumetric energy density is ≈0.48 kWh/L_{cell} (see Fig. 8). This is reasonably consistent with the battery-system projections for graphite/NMC111 by Gallagher et al.,[11] amounting to ≈0.19 ± 0.03 $kWh_{name\text{-}plate}/kg_{battery\text{-}system}$ (see Lithium ion battery status and expected advances section) and ≈0.42 ± 0.04 $kWh_{name\text{-}plate}/L_{battery\text{-}system}$. Quite clearly, due to the weight/volume contribution from the non-active cell components (separator, current collectors, etc.), the achievable cell-level energy densities strongly depend on the areal capacity and would still increase by ≈15% if the areal capacity can be increased from 2 to 4 mAh/cm^2 (see Figs. 7 and 8). Consequently, future automotive design targets focus on areal capacities of ≈4 mAh/cm^2, which should be feasible considering that the required

Table V. Specifications for NMC111 and Li_2S cathodes used for the cell-level energy density projections based on the pouch cell design described in Table IV.

NMC111 cathode		
content of NMC/ carbon/binder		94/4/2%wt.
active material capacity	theoretical	278 mAh/g_{NMC}
	practical	149 mAh/g_{NMC}
	utilization	53.6%
capacity of electrode coating		140 $mAh/g_{electrode}$ variable $mAh/cm^2_{electrode}$
electrode porosity		35%
Li_2S cathode with 60%wt sulfur content ("Li_2S_{low}")		
content of Li_2S/carbon/binder		68/24/8%wt.
Li_2S density		1.64 g/cm^3
active material capacity	theoretical	1166 mAh/g
	practical	933 mAh/g
	utilization	80%
capacity of electrode coating		634 $mAh/g_{electrode}$ variable $mAh/cm^2_{electrode}$
electrode porosity		35%

Table VI. Specifications for graphite, silicon, and metallic lithium anodes used for the cell-level energy density projections based on the pouch cell design described in Table IV.

graphite anode		
content of graphite/ carbon/binder		95/2/3%wt.
graphite density		2.25 g/cm^3
cell voltage	NMC111	3.7 V
	Li_2S	2.05 V
active material capacity	theoretical	372 mAh/g
	practical	353 mAh/g
	utilization	95%
capacity of electrode coating		336 $mAh/g_{electrode}$ variable $mAh/cm^2_{electrode}$
electrode porosity		35%
silicon anode with 1000 $mAh/g_{electrode}$ ("Si_{low}")		
content of silicon/carbon/binder		35/50/15%wt.
silicon density		2.34 g/cm^3
cell voltage	NMC111	3.47 V
	Li_2S	1.90 V
active material capacity	theoretical	3580 mAh/g ($Li_{15}Si_4$)
	practical	2860 mAh/g
	utilization	80%
capacity of electrode coating		1000 $mAh/g_{electrode}$ variable $mAh/cm^2_{electrode}$
electrode porosity		35%
metallic lithium anode (assumed anode/cathode capacity ratio of 2/1)		
content of lithium		100%wt.
lithium density		0.53 g/cm^3
cell voltage	NMC111	3.75 V
	Li_2S	2.10 V
active material capacity	practical	3860 mAh/g
capacity of electrode coating		3860 $mAh/g_{electrode}$ variable $mAh/cm^2_{electrode}$

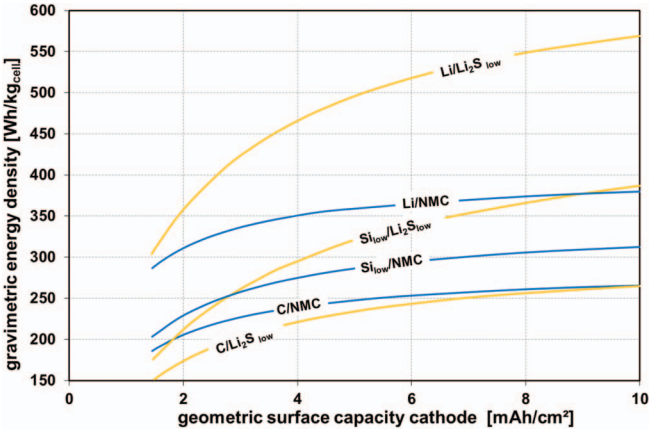

Figure 7. Cell-level gravimetric energy density comparison between sulfur and NMC based systems with different anodes as a function of geometric surface capacity. Cell and electrode specifications are given in Tables IV–VI.

power/energy ratio (viz., the maximum C-rate) for long-range BEVs with >50 kWh$_{name\text{-}plate}$ of available battery energy (see Table I) would be ≈2–4 h^{-1}.[12]

The comparison of graphite/NMC111 with graphite/Li$_2$S$_{low}$ ("Li$_2$S$_{low}$" referring to a Li$_2$S cathode with 60 wt% sulfur as specified in Table V) in Figure 7 shows that the gravimetric energy density of the latter is actually inferior throughout the entire feasible areal capacity range, which is largely due to the low cell potential of the graphite/Li$_2$S system. Therefore, while high cycle stability was demonstrated by Brückner et al.[71] for a lithium-sulfur battery with a graphite anode, it most definitively would not enable specific energies better or even equal to that of current LiB systems. Cell-level gravimetric energy densities superior to LiBs would only be possible for high-capacity anodes like silicon/carbon composites (referred to as "Si$_{low}$" with 1000 mAh/g$_{electrode}$ as specified in Table VI), and a comparison between Si/NMC111 and Si/Li$_2$S shows that Si/Li$_2$S system would enable higher cell-level specific energies at areal capacities higher than ≈3 mAh/cm^2 (see Fig. 7). Only with metallic lithium anodes, the cell-level gravimetric energy density of lithium-sulfur batteries (Li/Li$_2$S$_{low}$ in Fig. 7) would substantially exceed those of Si/NMC (by ≈70% at 4 mAh/cm^2) and of Li/NMC (by ≈35% at 4 mAh/cm^2), whereby the latter should be the more relevant comparison, since if one were to succeed using metallic lithium anodes in lithium-sulfur batteries its use should also be possible in LiBs (note, however, that the weight of the likely necessary diffusion barrier between the cathode and the lithium metal anode has not been included in these projections). For lithium-sulfur batteries with metallic lithium anodes, cell-level gravimetric energy densities of ≈350 Wh/kg$_{cell}$ have already been achieved.[72] To reach higher gravimetric energy densities, a reduction of electrolyte excess, increased sulfur weight fractions, and increased sulfur loadings would be required, as was recently pointed out by Eroglu et al.[69] and by Hagen et al.[70] The challenge here is to maintain sufficient rate capability with increasing sulfur loadings, since most of the publications so far have sulfur weight fractions of only ≈50 %wt and sulfur loadings of only up to ≈2.3 mg/cm^2 (≡3.9 mAh/cm^2) as reviewed by Hagen et al.[70]

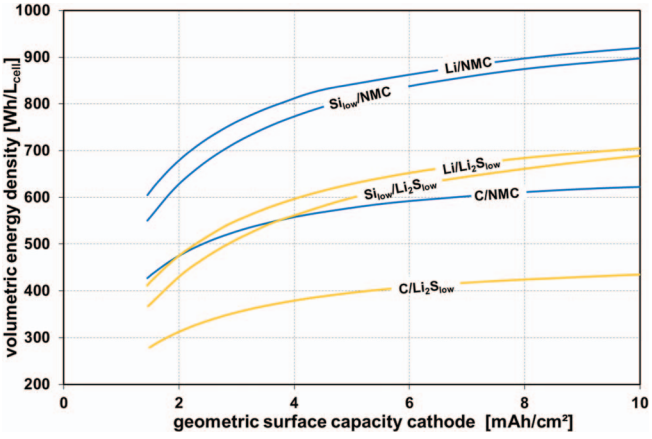

Figure 8. Cell-level volumetric energy density comparison between sulfur and NMC based systems with different anodes as a function of geometric surface capacity. Cell and electrode specifications are given in Tables IV–VI. The total cell energy can be obtained by multiplying the here shown volumetric energy density by the cell volume of 0.3 L (see Table IV), i.e., it ranges from ≈0.09 to ≈0.27 kWh$_{cell}$.

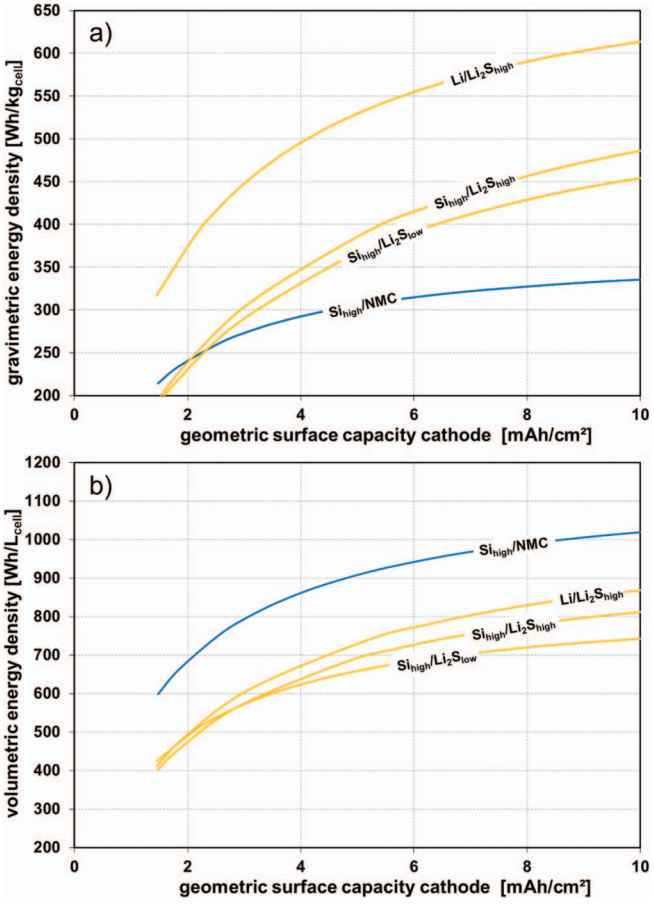

Figure 9. Cell-level a) gravimetric and b) volumetric energy densities of lithium-sulfur batteries with different combinations of low/high-capacity silicon anodes (Si$_{low}$ ≡ 1000 mAh/g$_{electrode}$ (see Table VI); Si$_{high}$ ≡ 2000 mAh/g$_{electrode}$ (see Table VII)) and low/high sulfur-content cathodes (Li$_2$S$_{low}$ ≡ 60 wt% S (see Table V); Li$_2$S$_{high}$ ≡ 70 wt% S (see Table VII)). The Si$_{high}$/NMC system is shown for comparison. Cell specifications are given in Table IV.

In conclusion, it is difficult to achieve the gravimetric energy density from a lithium sulfur battery-system which was expected based on the prognosis over the last few years. Along with that, the requirements of the automotive industry have also changed over the years, with increased focus on volumetric energy density rather than only gravimetric energy density. As is shown in Figure 8, the achievable volumetric energy densities for lithium—sulfur batteries, independent of the anode, will always be substantially lower than that of lithium ion batteries.

Slightly higher energy densities could be achieved by more aggressive targets for Si/C-composite anode capacities (areal capacity of 2000 mAh/g$_{electrode}$ for "Si$_{high}$", see Table VII) and for sulfur based

Table VII. Specifications for NMC111 and Li_2S cathodes used for the cell-level energy density projections based on the pouch cell design described in Table IV.

Li_2S cathode with 70%wt sulfur content ("Li_2S_{high}")		
content of Li_2S/carbon/binder		77/18/8%wt.
Li_2S density		1.64 g/cm^3
active material capacity	theoretical	1166 mAh/g
	practical	933 mAh/g
	utilization	80%
capacity of electrode coating		718 mAh/$g_{electrode}$
		variable mAh/cm$^2{}_{electrode}$
electrode porosity		35%
silicon anode with 2000 mAh/$g_{electrode}$ ("Si_{high}")		
content of silicon/ carbon/binder		70/20/10%wt.
silicon density		2.34 g/cm^3
cell voltage	NMC111	3.47 V
	Li_2S	1.90 V
active material capacity	theoretical	3580 mAh/g ($Li_{15}Si_4$)
	practical	2860 mAh/g
	utilization	80%
capacity of electrode coating		2000 mAh/$g_{electrode}$
		variable mAh/cm$^2{}_{electrode}$
electrode porosity		35%

cathodes (77 %wt Li_2S or 70 %wt S for "Li_2S_{high}", see Table VII). The critical technical aspect in this case is the high required silicon content (≈70 %wt), which at least currently typically display lower cycling stability, and it is yet unclear whether cathodes with such high sulfur content could have sufficiently high rate capability. If these high loadings could be realized, the resulting specific energy of this system (Si_{high}/Li_2S_{high} in Fig. 9a) would be ≈20% higher than that of a Si_{high}/NMC111 system at 4 mAh/cm^2 areal capacity; nevertheless, its volumetric energy density would still be ≈25% lower. These in the best case marginal gains of lithium-sulfur batteries (except if one were to succeed to use metallic lithium anodes) along with its so far poor cycling stability, lithium-sulfur batteries are currently considered unfeasible for use in passenger cars, particularly considering the challenging automotive requirements. Based on the current analysis and understanding, the main interest remaining in this system for the automotive industry is a potential material cost advantage.

Lithium-sulfur battery performance.— As evidenced by Figs. 7–9, high areal capacities are a prerequisite for obtaining competitive cell-level specifc energies for litiium-sulfur batteries. However, the rate capability for high sulfur loadings (i.e., high areal capacities) generally is very poor, and the recent study by Busche et al.[73] shows that the capacity of Li/S-cells decreases substantially at C-rates above 0.2 h^{-1}, despite their modest sulfur loadings (1.75 mg$_S$/cm^2, corresponding to ≈2.9 mAh/cm^2) compared to the ≥4 mAh/cm^2 which would be required to yield specific energies competitive with LiBs. In comparison, Figure 10 shows the rate capability and the cycle-life of Li/S-cells with ≈4 mAh/cm^2 and 58 %wt sulfur cathodes with a conventionally used electrolyte composed of DOL/DME (dioxolane/dimethoxyethane) with LiTFSI salt. Similar to Busche et al.,[73] substantially lower capacities are obtained at C-rates of ≥0.5 h^{-1} compared to ≤0.1 h^{-1}. Whether this is due to kinetic limitations of the sulfur electrode or whether the rate might also be compromised by the lithium metal anode is not clear at this point. The latter is not unlikely, since the geometric current density of 2 mA/cm^2 at the C-rate of 0.5 h^{-1} (based on 4 mAh/cm^2) is probably already too large for the stable operation of a lithium foil-based anode in the absence of a an additional protective film between anode and cathode.[28,29,74]

To safely enable high geometric current densities, high-surface area anodes are advantageous, viz., high-surface area lithium metal powders[28] or silicon anodes using high-surface area silicon nanoparticles, for which no difference in the capacity of Si/Li_2S cells was observed between high current densities of 2.3 mA/cm^2 (≡ C-rate of

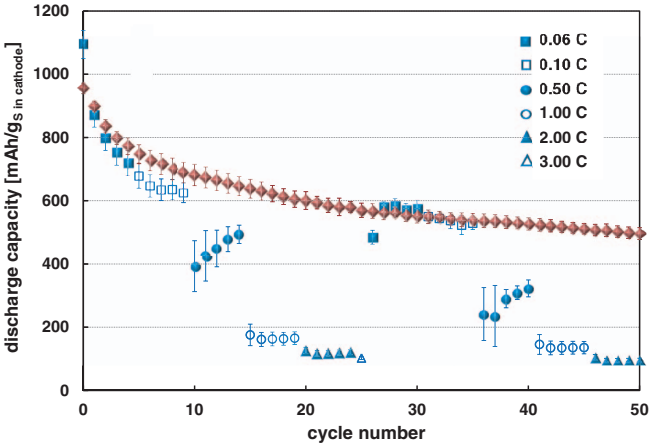

Figure 10. Cycling stability of sulfur cathodes (4.0–4.3 mAh/cm^2, 58 %wt sulfur) with metallic lithium-foil anodes tested either at a constant C-rate of 0.06 h^{-1} (red symbols) or with variable C-rate (blue symbols) between 1.5 and 2.6 V. Data were acquired with coin cells (1.13 cm^2) at 23°C, and error bars represent the standard deviation from three independent measurements. The electrolyte was composed of DOL/DME with LiTFSI salt.

1 h^{-1}) and more modest current densities of 0.46 mA/cm^2 (≡ C-rate of 0.2 h^{-1}).[75] As shown in Figure 11, the cycling stability of sulfur cathodes with electrochemically pre-lithiated silicon anodes is superior to cells with metallic lithium anodes without a protection layer, which is likely related to the absence of dendrite formation and to a more stable SEI formation with silicon anodes. However, ex-situ pre-lithiation of silicon anodes (i.e., prior to lithium-sulfur cell assembly) would likely be too complex for large-scale processiong, particularly in view of the high reactivity of lithium silicides. In-situ pre-lithiation using an added lithium source (e.g., metallic lithium particles[28]) would reduce handling complexity and might thus be a more feasible approach. The other option, of course, is the use of Li_2S- instead of S-cathodes,[75] which, however, would also require strict humidity control to avoid the formation of toxic H_2S gas during assembly.

In all cases, it should be noted that these additional methods result in additional costs, so that the advantage of using a lower-cost cathode active material such as sulfur is not evident anymore. A further possibility to decrease the cost of battery cells is the use of cheap graphite anodes in combination with sulfur cathodes. These cells show good

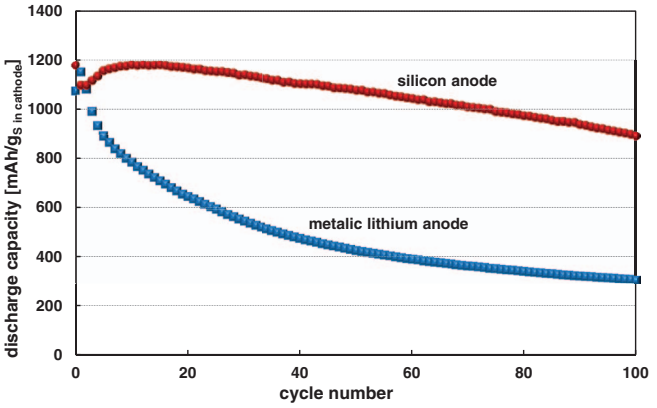

Figure 11. Cycling stability of sulfur cathodes (58 %wt sulfur) with either a metallic lithium-foil anode (blue symbols) or with a Si/C-composite anode with 20 %wt Si (red symbols), tested at a constant charge/discharge rate of 0.12 h^{-1} between 0.9 and 2.6 V. Data were acquired with coin cells (1.13 cm^2) at 23°C, and the Si/C-composite anode were electrochemically pre-lithiated prior lithium-sulfur cell assembly. The electrolyte was composed of DOL/DME with LiTFSI salt and additives (polysulfides and other additives). The silicon electrodes were provided by Wacker Chemie AG.

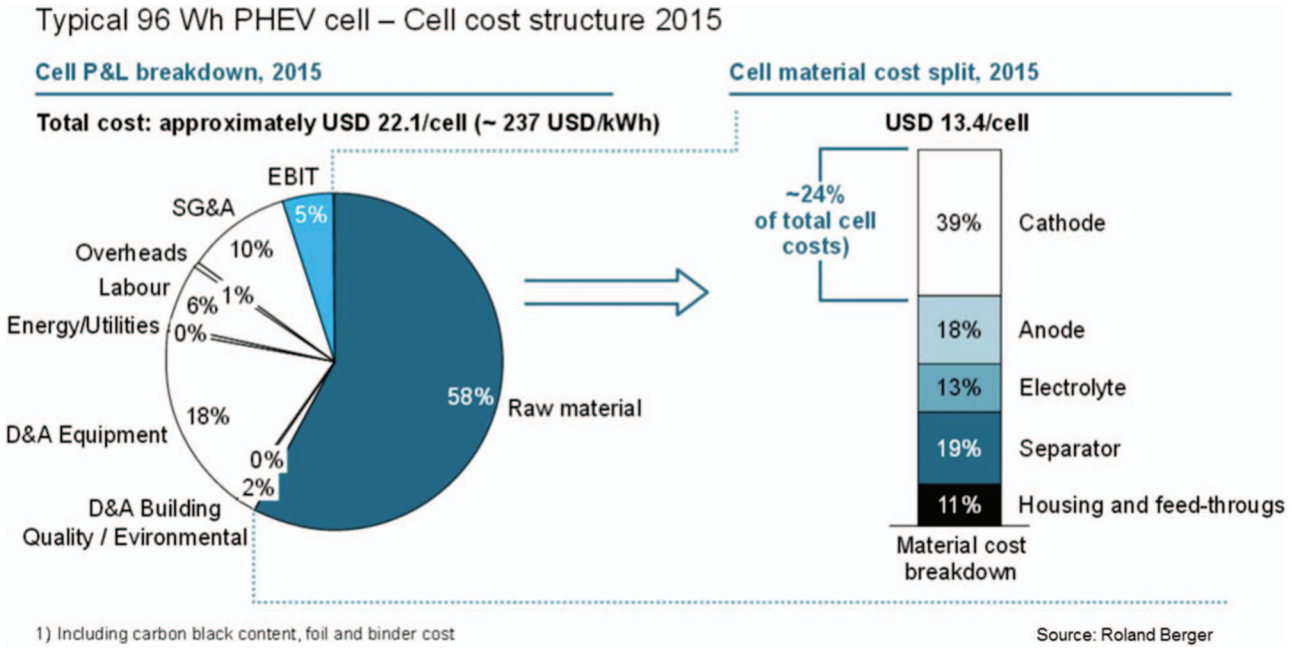

Figure 12. Cell and material cost for a PHEV battery based on lithium ion battery technology (graphite/NMC111) (Reproduced from[76] with permission from Roland Berger).

cycle performance, but the technology performance is not attractive, because of the low achievable energy density.

In conclusion, the system with silicon anodes has also a good cycle stability without the use of barriers such as solid electrolytes or polymers. Furthermore, silicon anodes do not form dendrites, which leads to a safety advantage. In addition there is evidence that the C-rate capability of cells with silicon anodes is higher than cells with lithium metal anodes.

Lithium-sulfur battery cost analysis.— The cost of battery cells is a crucial aspect, which could be favorable for lithium-sulfur batteries compared to LiBs: sulfur is a very low-cost material and its non-toxicity would ease the safety handling requirements during cell manufacturing. The potential cost advantage of sulfur as cathode material for a plug-in hybrid electric vehicle (PHEV) can be evaluated considering the diagrams in Figure 12 (from Reference 76). The raw material cost contributions to the total cost of a typical lithium ion battery cell are ≈58%, ≈39% of which are due to the cathode active material cost. Thus, the cathode active material cost accounts for ≈23% of overall battery cell cost based on a graphite/NMC111 based lithium ion battery.

Assuming that the cost breakdown of a battery cell with a metallic lithium anode is similar to that of a battery cell with a graphite anode, and considering that the price of sulfur is negligible compared to NMC111, one would project a cost advantage of ≈20% for a Li/Li_2S (or Li/S) battery cell. However, if one were to use a silicon anode in a lithium-sulfur battery, lithium has to be introduced by either using a Li_2S-cathode, by ex-situ pre-lithiation prior to cell assembly, or by in-situ pre-lithiation during battery formation using metallic lithium metal films or particles as lithium source. Unfortunately, up to now there are no cost predictions available for industrial-scale use of pre-lithiation methods, but it is clear that these processes will add cost, thereby reducing the above estimated cost benefit of lithium-sulfur batteries. In the case of metallic lithium anodes, protection layers (polymer/solid electrolyte) are likely required for safety and stability reasons, which will also add yet undefined cost. Further cost studies can be found in the analysis by Eroglu et al.[69]

Safety aspects of lithium-sulfur batteries.— Dendrite formation is a well-known risk with metallic lithium anodes, leading to internal short circuits and safety hazards. A possible solution could be the use of a lithium-conducting solid electrolyte, acting as barrier to prevent dendrite formation and to block polysulfide reduction and deposition on the anode surface. The company Oxis Energy, e.g., uses a ceramic lithium sulfide based passivation layer in combination with a non-flammable electrolyte to achieve a safe lithium metal battery.[77] On the other hand, dendrite formation is no concern with silicon anodes, but the safety of nanometer-sized silicon anodes, particularly in their lithiated state, is still an active area of research.

A drawback of the lithium-sulfur technology is the high reactivity of the Li_2S discharge product, which would form toxic H_2S in contact with moist air if the cell seal were break or rupture accidentally. On the other hand, the so far commonly used LiTFSI salt in lithium-sulfur batteries constitutes a safety advantage over $LiPF_6$ salt used in LiBs, as it does not release HF upon contact with moisture.

Lithium-sulfur battery technology for vehicle applications – summary.— To achieve cell-level gravimetric energy densities competitive with advanced LiBs (Si-anode and HE-NMC, nickel-rich NMC811, or NCA, see Lithium ion battery status and expected advances section), lithium-sulfur batteries would require relatively large areal capacities (≥4 mAh/cm^2) and high cathode sulfur content (≥60 %wt). Under this condition, lithium-sulfur batteries with silicon anodes could reach 350–400 Wh/kg_{cell} (see Fig. 9a), at best ≈1.3-fold larger than the values projected for advanced LiBs.[12] If one were to succeed with developing durable and safe lithium metal anodes, 450–500 Wh/kg_{cell} could be obtained with lithium-sulfur batteries (see Fig. 7), which again would at best ≈1.3-fold larger than the gravimetric energy densities for advanced LiB cathode materials coupled with lithium anodes.[12] In terms of volumetric energy density, lithium-sulfur battery cells are definitively inferior to LiBs. However, with regards to cost, lithium-sulfur batteries might be superior, if the additional components which might be needed to improve cycle-life and safety (diffusion barriers, etc.) can be realized at low cost. The use of silicon anodes instead of metallic lithium might enable higher power densities and longer cycle-life, if SEI-stabilizing electrolytes/additives can be developed which prevent the continuous consumption of electrolyte during cycling. One open issue with silicon anodes in lithium-sulfur batteries is the incorporation of lithium by either industrially feasible

pre-lithiation procedures or by the use of LiS- rather than S-cathodes for cell assembly.

So far, the lithium-sulfur system does not satisfy the battery power/energy requirements for BEV applications. However, the lithium-sulfur system is interesting for battery-powered vehicles with low power/energy requirements and for applications where power density and volume is less important than cost.

Hydrogen Fuel Cells – Materials Requirements and Durability

Besides the question of hydrogen generation and distribution briefly discussed in Cost and range estimates/constraints for all-electric vehicles section, the technical challenges toward FCEV commercialization are lowering fuel cell system cost and a reduction/elimination of platinum, expressed in terms of platinum-specific power density (g_{Pt}/kW). Pathways toward the latter are improved platinum-based catalysts for the oxygen reduction reaction (ORR) with increased mass activity (typically given as A/mg_{Pt} at reference conditions of 0.9 V, 100 kPa_{abs} O_2, and 80°C), catalysts free of platinum-group-metal (PGMs), and/or the development of MEAs (membrane electrode assemblies) which can operate at higher power density (i.e., at higher current density).

The fuel cell system long-term cost target set by the US Department of Energy (DOE) is 40 $/kW,[13] a number which was used in the FCEV cost projections shown in Table II. Various cost studies show that economy-of-scale effects will lead to lower fuel cell system cost, with the result that the fractional cost contribution for the MEA is expected to increase.[78,79] By 2020, the MEA cost targeted by the DOE is 17 $/kW.[80] With regards to MEA components, cost studies suggest that economy-of-scale effects will significantly reduce membrane cost (to 5–20 $/$m^2$),[78,81] ionomer cost (to 75–150 $/kg),[78,82] as well as gas diffusion layer (GDL) cost (to 4–11 $/$m^2$).[78] Under these conditions, the cost contribution from the currently used platinum based catalysts will dominate MEA cost, and even if the long-term DOE target for the platinum-specifc power density of 0.1 g_{Pt}/kW were to be reached, the platinum cost share of the MEA would amount to ≈40% (this assumes platinum costs of ≈48 $/$g_{Pt}$). Nevertheless, at the 0.1 g_{Pt}/kW level, the platinum cost for a 100 kW fuel cell stack would be manageable (≈480 $ for the 10 g_{Pt}/stack), and 10 g_{Pt}/FCEV would also be feasible with regards to platinum availability. Unfortunately, most state-of-the-art MEAs have platinum loadings (anode and cathode) of 0.4–0.5 mg_{Pt}/cm^2 and have been operated at maximum power densities of ≈1 W/cm^2 at cell voltages of ≈0.65 V, required to enable steady-state heat rejection by the vehicle cooling system.[83] For a 100 kW fuel cell stack per FCEV, this leads to an unacceptably high platinum demand of 50 g_{Pt}/FCEV. Therefore, lowering the amount of platinum through more active platinum-based catalysts and/or via increased MEA power density is a prerequisite for large-scale FCEV commercialization. It should be mentioned, that possible long-term alternatives to platinum-catalyst-based fuel cell technology would be: i) the replacement of platinum-based catalysts in PEM fuel cells by non-PGM catalysts (see below); or, ii) a transition to alkaline membrane fuel cells, for which sufficiently active non-PGM ORR catalysts are available, but for which there currently are no non-PGM hydrogen oxidation catalysts.[84] However, at the current time, the maturity level of these two technologies, particularly of the latter, is still far from sufficient for use in hydrogen-powered FCEVs.

Despite these challenging targets, the market introduction by Toyota and Hyundai/Kia suggests that FCEV technology, at least in the view of these OEMs, is sufficiently mature to not only last an automotive life span, but that there also might be a viable pathway to ultimately meet catalyst cost/availability targets. In the case of Toyota's FCEV "Mirai", the required amount of platinum was likely reduced by increasing the power density of the fuel cell stack, as is suggested by Figure 13, comparing schematically the polarization curves of their 2008 FCEV vs. their 2015 Mirai model.[85] In addition, the platinum ORR catalyst was replaced by a platinum-cobalt alloy, with an 1.8-fold higher mass activity compared to platinum.[85] While actual platinum loadings are not stated, it is likely that they are somewhat reduced

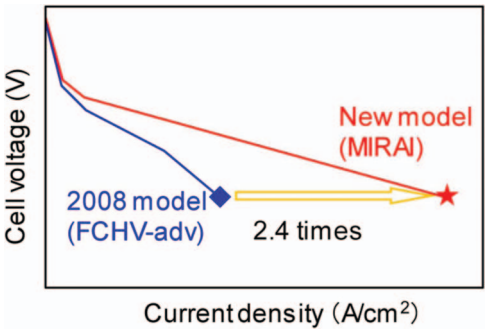

Figure 13. Schematic comparison of the fuel cell stack polarization curves of the 2008 model FCEV ("FCHV-adv") and the Mirai FCEV. (Reproduced from Konno et al.[85] with copyright © 2015 SAE International. Further use is not permitted.)

compared to Pt-only MEAs (≈0.4–0.5 mg_{Pt}/cm^2 $_{MEA}$[83]) to probably ≈0.35–0.4 mg_{Pt}/cm^2 $_{MEA}$. Under the assumption that the polarization curves in Figure 13 are based on real data and that the current density in the 2008 FECV stack was ≈1–1.25 A/cm^2 at ≈0.5–0.6 V, the Mirai FCEV would operate between ≈2.4–3.0 A/cm^2, resulting in power densities of ≈1.2–1.8 W/cm^2. Thus, for the 114 kW fuel cell stack in the Mirai, the estimated amount of platinum in the fuel cell stack would lie somewhere in the range of 38 to 22 g_{Pt} (corresponding to ≈0.33 to ≈0.19 g_{Pt}/kW). At the same time, if the above estimates are correct, the active surface area of the 114 kW stack would have been reduced from ≈11.4 m^2 at previously ≈1 W/cm^2 to ≈9.5–5.6 m^2 (≈1.2–1.8 W/cm^2), corresponding to ≈17–44% cost savings for the membrane, the GDL, and the bipolar plate. The key MEA concepts which according to Toyota enabled the high current densities in the Mirai stack are:[85] i) a "solid-carbon" catalyst-support, which improves operation at low relative humidity due to the location of Pt particles on the outer surface of the carbon-support rather than in its interior;[86] ii) thin membranes, in the range of ≈10 μm, improving water equilibration across the membrane at high current densities and lowering protonic resistance; iii) ionomers in the catalyst layers with high ion exchange capacity to improve catalyst utilization; and, iv) thin gas diffusion layers (probably ≈100−150 μm) and microporous layers with bigger pores to enhance water and gas transport. Other than the MEA, the main feature permitting high current density operation is reported to be a new cathode flow-field structure ("3D fine-mesh"), with claimed improved water removal and high gas permeability. In addition, the fine-pitch serpentine-flow anode flow-field with improved stamping design enables higher compressive forces, resulting in lower contact resistance.[87] The counter-current H_2/air flow operation afforded by the serpentine-flow anode flow-field in combination with the split-flow air flow-field design eliminate the need for inlet-air humidification, thereby further reducing mass transport losses at high current density.

Approaches to increase catalyst activity.— While increasing power densities by using thinner membranes and GDLs, more conductive ionomers in the electrode, and improved flow-fields are critical elements toward cost reduction and reduction of platinum content, the ultimate goal of platinum-specific power densities of 0.1 g_{Pt}/kW requires further improvements of the mass activity of platinum-based ORR catalysts. The US DOE[80] defined a mass activity target of 0.44 A/mg_{Pt} at 0.90 V iR-free voltage (defined at 80°C with 150 kPa_{abs} fully humidified hydrogen/oxygen), often referred to as the "4x ORR catalyst", while the Japanese FCCJ (Fuel Cell Commercialization Conference of Japan) aims for an even more aggressive mass activity goal of a 10-fold improvement over a conventional 50 wt% platinum catalyst supported on high-surface area carbon, viz., 1.0 A/mg_{Pt}.[88] In contrast to the low ORR activity of platinum, its activity for the HOR with pure hydrogen is very high, so that the anode platinum loading has a rather small impact on the overall platinum loading of the MEA. At anode Pt loadings as low as 0.025 mg_{Pt}/cm^2, the expected HOR

kinetic overpotential loss (80°C and 100 kPa_{H2}) for a Pt catalyst with a dispersion of 50 m^2/g_{Pt} would only amount to ≈16 mV at 3 A/cm^2 (i.e., at 120 A/mg_{Pt}) based on its high HOR exchange current density (≈0.5 A/cm^2_{Pt} at a Tafel slope of ≈140 mV/decade).[89] Thus, catalyst development for H_2-fed PEM fuel cells is focused on cathode catalysts and will be briefly reviewed in the following; for detailed reviews, the interested reader is referred to recent review articles.[90,91]

The most widely employed strategy to increase mass activity is the dispersion of Pt nanoparticles on high-surface area carbon blacks. Platinum has long been known to be the most active metal for the electrochemical reduction of oxygen. Already in the 1980s, Appleby plotted the experimentally determined adsorption potentials of adsorbed surface O or OH species (determined by cyclic voltammetry) for a large number of different metals vs. their specific activity (i.e., the activity referenced to the exposed metal surface area) for the oxygen reduction at 0.80 V and found that it followed a volcano plot shape, with Pt being most active.[92] Later on, the binding energy of O and OH with metal surfaces was calculated via DFT (density functional theory) by Nørskov et al. and plotted vs. the calculated ORR activities based on a dissociative oxygen reduction mechanism.[93] This resulted in a similar volcano plot, with platinum being close to the top, suggesting that for too low O/OH-binding energy (as in the case of gold), the oxygen-oxygen bond cannot be cleaved, while too strong O/OH-binding energy (e.g., in the case of tungsten), the reaction intermediates cannot desorb. The O/OH-binding energy is rather close to optimum in the case of platinum, which rationalizes its high ORR activity. Unfortunately, the mass activity increase with reduced Pt size which would be predicted by the inverse proportionality of the exposed electrochemically active surface area (ECSA) with Pt particle size, is generally not observed due to the so-called particle-size effect, namely the observation that the specific activity decreases with decreasing Pt particle size to approximately a tenth of that of so-called extended surfaces (i.e., bulk platinum).[94] With a few exceptions, most researchers believe that the adsorption strength of adsorbed oxygenated species such as O/OH intermediates increases as the particle size decreases. This is supported by DFT calculations, which found that the increasing number of low-coordinated sites (i.e., edge and corner sites) on increasingly smaller Pt nanoparticles lead to increased O/OH-binding energies and hence reduce the ORR activity.[95] These observation limit the ORR mass activity of state-of-the-art highly dispersed Pt nanoparticles supported on high-surface area carbon blacks to ≈0.18 A/mg_{Pt}.

Alloying Pt with base metals such as Fe, V, Co, Ni, Cu, Cr, and Ti was shown to increase the specific activities for the oxygen reduction reaction;[96,97] more recently, Pt-Y alloys have also reported to show high specific activity in rotating disk electrode (RDE) measurements,[98] but have not yet been validated in MEAs. Reasons for increased specific activity of Pt-alloys are still under discussion and are hypothesized to be due to either the change of the Pt-Pt interatomic distance facilitating the O-O bond cleaving,[99] to lattice strain effecting a downshift of the d-band center, or to the so-called ligand effect.[100] Stamenkovic et al. showed that the experimentally and the calculated d-band center correlates well with the specific activities of Pt_3Ti, Pt_3V Pt_3Fe, Pt_3Co, Pt_3Ni, and polycrystalline Pt,[101,102] consistent with the long known role of the d band in determining the O/OH adsorption energy[103] and in accordance with the later calculations by Hammer and Nørskov.[104] Stamenkovic et al. also report that annealed Pt-alloy surfaces show higher ORR activity, related to the so-called "Pt-skin" formation, while sputtered and subsequently acid leached samples formed "Pt-skeleton" surfaces with lower activities.[102] In the case of the annealed surfaces, a second layer enriched with the alloy component was identified and is believed to be responsible for the higher activity.[101] The most active alloys were Pt_3Fe, Pt_3Co, and Pt_3Ni. Stamenkovic et al. also found that the annealed surface of $Pt_3Ni(111)$ single crystals shows a uniquely high specific activity, exceeding that of bulk Pt by a factor of ≈10,[105] which triggered many studies on the synthesis of shape-controlled Pt_3Ni nanoparticles (see below). The concept of Pt-skin and Pt-skeleton type catalysts has also been found to apply to carbon-supported Pt_3Co nanoparticles,[106] which upon annealing exhibit Pt-rich skins (≈3 monolayers) with ≈4-fold times higher specific activity. Up to 2009, reported mass activities of commercial Pt-alloy catalysts were in the range of 0.2 to 0.3 A/mg_{Pt},[107] showing an up to ≈3-fold enhancement over pure Pt.

A new class of Pt-alloy catalysts was introduced by Strasser's group, with catalysts prepared from base metal rich precursors (PtM_x, with $x \geq 1$), initially using copper which was electrochemically dealloyed in the final step of catalyst preparation.[108,109] The dealloyed catalysts showed mass activities exceeding the DOE target of 0.44 A/mg_{Pt}, but their durability during accelerated voltage-cycling tests of MEAs was poor, since copper was leached from the cathode catalyst and deposited on the anode side.[110] The dealloying concept was then further refined, starting from Pt-alloys that are rich in other base metals such as $PtNi_3$ and $PtCo_3$, resulting in mass activity enhancements of up to a factor of 6 to 7 compared to pure Pt.[111] Furthermore, for practical reasons, electrochemical dealloying was replaced by acid leaching,[112] which has ultimately resulted in carbon-supported dealloyed Pt-Ni catalysts with mass activities as high as ≈0.64 A/mg_{Pt}.[113] The most stable catalyst was a sulfuric acid leached and subsequently annealed (400°C) sample, with an unprecedentedly high mass activity of ≈0.55 A/mg_{Pt} remaining after an accelerated voltage-cycling aging test (30,000 potential cycles between 0.6 to 1 V). According to the authors,[113] the catalyst precursor was produced by a scalable process route, so that this technology will likely find its way into FCEVs in the very near future.

Another interesting class of ORR catalysts has been presented by 3 M with their nanostructured thin film catalyst (NSTF) concept. There, Pt or Pt-alloys are physical vapor deposited on an organic crystalline substrate derived from perylene red (N, N-di(3,5-xylyl)perylene-3,4:9,10 bis(dicaroximide)), which self-assembles upon annealing into so-called "nano-whiskers" with dimension of around 25 nm x 25 nm x 0,5–2 μm.[114] While the NSTF approach yields metal dispersions of only 10–25 m^2/g_{Pt}, due to the extended crystals grown on the whiskers, specific activities determined in MEAs are as high as 2.5 mA/cm^2_{Pt}, with concomitant mass activities of up to 0.5 A/mg_{Pt}.[114] Key advantages are high mass activity and excellent durability at high anodic potentials occurring during start/stop events or during cell reversal, since the whiskers have very high anodic corrosion stability.[114] Unfortunately, the poor performance of NSTF electrodes at low operating temperature (<50°C) when liquid water is present as well as during freeze-starts due to its low ice-storage capacity has so far prevented their use in vehicle fuel cell stacks.

Besides (dealloyed) Pt-alloys and the NSTF approach, the Pt mass activity could in principle also be increased by depositing of monolayers of Pt on less expensive core materials. Theoretically, a Pt monolayer would offer a Pt dispersion of 235 m^2/g_{Pt}, which may be compared to carbon-supported Pt nanoparticles with typically less than 120 m^2/g_{Pt}.[94] Adzic et al. utilized this principle and invented Pt monolayer (ML) core-shell catalysts on different core materials prepared by a Cu displacement method, such as Pt_{ML}/Au/Ni, Pt_{ML}/Pd/Co, and Pt_{ML}/Pt/Co.[115] The reported Pt mass activity gain measured in RDE experiments was ≈10-fold. Together with Johnson Matthey, a scalable synthesis route for Pt_{ML}/PdCo/C was developed,[116] leading to core-shell catalysts with a mass activity of 0.72 A/mg_{Pt} demonstrated in RDE measurements. However, long-term stability in MEAs, particularly under voltage-cycling conditions, still needs to be proven and seems rather challenging considering the fact that transient platinum dissolution will occur during voltage-cycling.

Finally, the remaining known class of Pt-based ORR catalysts with potentially very high mass activity are the so-called shape-controlled Pt-alloys, which utilize processes aiming to synthesize nanoparticles with preferential orientation as reviewed for example in Reference 117. Carpenter et al. reported the synthesis of Pt_xNi_{1-x} prepared by a solvothermal synthesis using N,N dimethylformamide (DMF) as solvent and reducing agent.[118] Depending on alloy composition, they found cubic, cuboctahedral (Pt_3Ni), octahedral and truncated octahedral (Pt_1Ni_1) particle shapes. The latter Pt_1Ni_1 particles yielded mass activities of up to 0.68 A/mg_{Pt} in RDE experiments.

Later on, Cui et al. synthesized shape-controlled Pt_xNi_{1-x} octrahedra by a similar DMF-based solvothermal method and followed their structural changes during electrochemical dealloying.[119] They report RDE derived mass activities of up to ≈1.5 A/mg_{Pt} for electrochemically activated samples, which is surprisingly close to a simple back-on-the-envelope prediction made several years ago.[120] The most recent example of shape-controlled particles combined with dealloying is the study by Chen et al., preparing "multimetallic nanoframes" by dealloying $PtNi_3$ polyhedra, which after annealing form Pt(111) skin type Pt_3Ni structures.[121] RDE characterization showed extraordinarily mass activities, exceeding that of Pt/C catalyst by a factor of 22 and indicated good voltage-cycling stability (10,000 cycles between 0.6 and 1 V). While promising, MEA performance and durability datas for shape-controlled catalysts are still missing, and it remains to be seen whether they will retain their morphology during extended voltage-cycling at higher temperatures and whether volume manufacturing of shape-controlled catalysts is feasible.

A number of non-PGM approaches have been presented such as doped valve metal oxides[122] as well as carbon and nitrogen coordinated iron or cobalt (Fe/Co-N-C).[124] So far, only the activity of the latter is promising, and their development progress has been extraordinary, reaching Pt/C type turnover frequencies and H_2/O_2 fuel cell performance curves matching Pt/C at low current densities up to ≈10 mA/cm^2.[123,124] The power densities achieved with H_2/air fuel cells are ≈0.15 W/cm^2 and it has been shown that the performance remains reasonably stable over ≈100 h.[123] While these results are promising for future generations of fuel cells, the power density achievable with non-PGM catalysts is still ≈10-fold too low and their durability is still not sufficient for the upcoming generations of fuel cell vehicles.

Figure 14 depicts the above described advances in platinum group catalysts versus time. ORR catalysts meeting the 2020 DOE mass activity target of 0.44 A/mg_{Pt} are actually available (see green circle). Concepts for even further increased mass activity, viz., shape-controlled catalysts (white hexagon) have been demonstrated in RDE measurements, but MEA performance and durability tests are still lacking.

Catalyst durability.— Under automotive conditions, transients such as start/stop events and load variations inducing voltage-cycling lead to the degradation of both the carbon-support ("carbon corrosion") and the active metal phase (metal dissolution/sinterting). The following catalyst degrading events are the most prevalent: i) load variations due to varying vehicle power demand, leading to potential cycling of the ORR catalyst between ≈0.7 and ≈0.9 V;[81] ii) conditions where no current (open-circuit voltage (OCV) conditions at ≈0.95 V) or little current (idle conditions at ≈0.90 V) is drawn in H_2/air (anode/cathode) environment or at OCV in air/air environment (during the passing of an air-front through the anode at start/up, resulting in ≈1.05 V);[116,125] iii) start/stop events during which a H_2/air-front passes through the anode, leading to cathode potentials ≫1 V;[126] iv) local fuel starvation within a single cell, leading to similarly high cathode potentials;[127] and, v) cold starts with ill-distribution of the H_2 fuel in the stack, with individual cells being supplied with a H_2 stoichiometry below one which leads to cell reversal.[128] Generally the loss of catalyst functionality and hence MEA performance is caused by either ECSA loss (mostly during voltage-cycling) and/or carbon corrosion (mostly at cathode potentials ≫0.9 V).

Loss of Pt electrochemical surface area.—In principle, Pt surface area loss during potential cycling may proceed via three routes: i) dissolution of Pt with re-deposition either in the ionomer phase (Pt band formation) or on bigger particles (Ostwald ripening); ii) surface detachment of Pt particles, leading to electronically disconnected and thus inactive platinum particles; and, iii) particle coalescence caused by carbon corrosion and/or particle surface migration. Detailed discussions can be found in Reference 129 and in a more recent review by Kocha.[130] A material solution known to reduce ECSA loss during potential-cycling is the increase of platinum(-alloy) particle size and/or high-temperature annealing of the catalyst.[125] The ECSA loss over the expected 300,000 voltage cycles between 0.70 and 0.90 V (iR-free voltage) during automotive life can be estimated by an extrapolation of the voltage-cycling data over the first 30,000 cycles,[81] suggesting that it might be possible to reach the DOE targets for voltage-cycling induced ECSA and mass activity losses with (annealed) Pt-alloys. However, in general FECV system designers seek to minimize voltage-cycles by hybridization of the fuel cell system with a high-power battery.[3]

With optimized dealloyed PtNi/C catalysts reported by Han et al., the ORR mass activities change very little over 30,000 voltage cycles (see samples P2-SA-AN, P2-SA, and P2-NA shown in Figure 15), even though non-negligible ECSA losses have been observed.[113] In the same figure, they show that the "Supplier Pt Alloy" catalyst, presumably a commercial catalyst, is also very close to the DOE

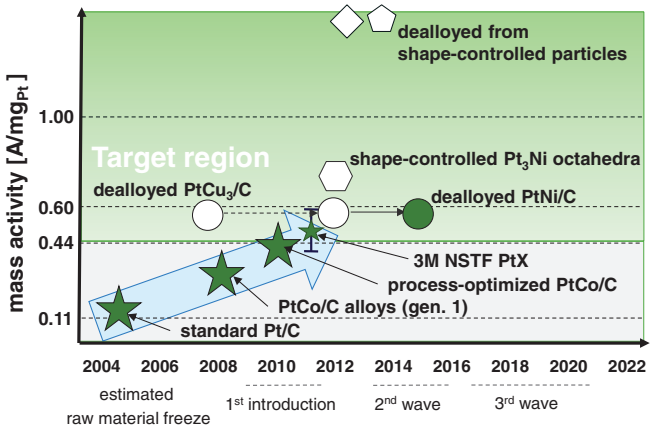

Figure 14. Schematic of reported MEA mass activities (full figures) of Pt-based ORR catalysts appearing viable for mass manufacturing (green symbols) and interesting PGM-based concept catalyst showing promising RDE and in some cases MEA based mass activities (white symbols). Standard Pt/C, PtCo/C alloys (gen. 1),[107] process-optimized PtCo/C (gen. 2), dealloyed $PtCu_3$,[109] 3M NSTF,[114] dealloyed PtNi/C[113] and catalysts derived from dealloyed shape-controlled Pt-alloy particles.[119,121] At the bottom of the figure are the estimated material design freeze periods for FCEVs which have been introduced today (2010 to 2012), for the fast-follower's FCEV introduction in 2017 to 2020 (2014 and 2016), and for the first wave during market expansion in 2020+ (around 2018+).

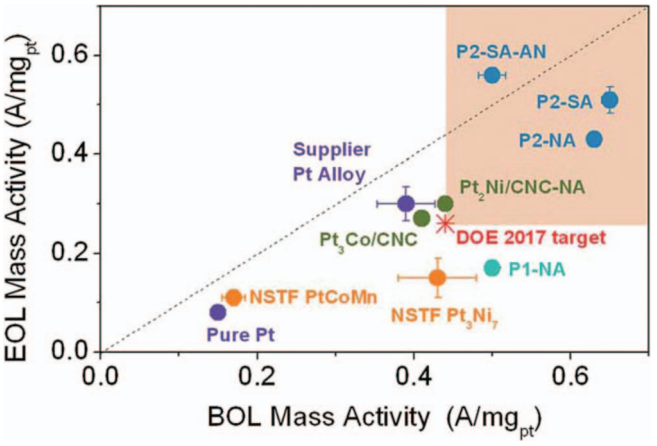

Figure 15. Beginning-of-life (BOL) vs. end-of-life (EOL) catalyst mass activities (at 0.90 V (iR-free), 80°C, and 150 kPa_{abs} of O_2 at 100% relative humidity) measured before and after voltage-cycling experiments (30,000 voltage cycles of the cathode between 0.6 to 1.0 V at 50 mV/s in fully humidified H_2/N_2 at 80°C) at GM. The chemically dealloyed PtNi/C catalysts (P2-SA-AN, P2-SA, P2-NA) exceed the DOE mass activity and stability target. (Reproduced from Han et al.[113] with permission from the Royal Society of Chemistry.)

target (see red asterisk in Fig. 15) of 0.44 A/mg_{Pt} at beginning-of-life (BOL) and of 0.25 A/mg_{Pt} at end-of-life (EOL). Unfortunately, ECSA losses of Pt-alloys are generally accompanied by the release of the 3d transition metals into the ionomer phase,[94,131] where they can have a detrimental effect on MEA performance as they reduce ionic conductivity and, more importantly, lead to increased voltage losses due to cation gradients in the MEA.[132] Therefore, the total molar amount of leachable transition metals over the life-time of the MEA must be kept small compared to the total proton inventory of the membrane and the catalyst layers ($\ll$10%).[132]

In the literature, a few other approaches to maintain ECSA during voltage-cycling have been discussed. Zhang et al. prepared Pt/C catalyst decorated with gold clusters,[133] which are claimed to raise the Pt oxidation potential and thus to increase voltage-cycling stability; this was demonstrated by RDE measurements, but has not yet been validated in MEAs. Another interesting concept has been presented by Matsumori et al., who covered the Pt catalyst surface with a thin SiO_2 film,[134] reporting significant stability improvements in terms of ECSA loss during voltage-cycling between 0.05 and 1.2 V, measured in an RDE configuration. A similar concept has been presented recently by Cheng et al., who encapsulated carbon nanotube-supported Pt by ZrO_2 using ALD (atomic layer deposition).[135] The most active and stable sample (annealed at 600°C after ALD) showed BOL mass activities of 0.28 A/mg_{Pt}, which remained almost unchanged during 4,000 cycles between 0.6 and 1.2 V.

Carbon-support corrosion.—As outlined above, high cathode potentials occur during idle or open-circuit conditions in H_2/air operation ($\approx$0.90 V and $\approx$0.95 V, respectively), under air/air ($\approx$1.05 V) during start/stop phases, as well as during local fuel starvation or unmitigated start/stop transients ($\gg$1 V). At these high potentials, carbon is oxidized to CO_2 and CO, leading to structural changes in the catalyst layers and to large performance losses once $\approx$5–10 wt% of the carbon is oxidized.[125] Figure 16a shows the extent of carbon corrosion vs. time at the different voltages estimated from the carbon corrosion kinetics of commonly used high-surface area non-graphitized carbon-supports, indicating that even during idle operation of the vehicle ($\approx$0.90 V), substantial carbon corrosion might occur during vehicle life. This becomes even more pronounced at OCV and during air/air phases, so that fuel cell operation without applied load (i.e., at OCV) and fuel cell storage under air must be minimized. Since carbon corrosion rates are inversely proportional to BET surface area and decrease with increasing degree of graphitization,[136,137] low-surface area carbon-supports, frequently graphitized, are more and more utilized to increase catalyst durability.[85]

At the very high anodic potentials caused by the passage of a H_2/air-front through the anode flow-field during so-called unmitigated start/stop events,[126,137] carbon corrosion is very rapid, leading to substantial MEA performance losses over very few start/stop cycles. An accelerated start/stop durability test is shown in Figure 16b, demonstrating the rapid H_2/air performance losses when H_2/air-fronts with a residence time of 1.3 s are sent through a fuel cell using MEAs containing platinum supported on a standard carbon-support (i.e., a high-surface area carbon with $\approx$600 m^2/g BET area). The degradation at high current density is severe, and no power can be delivered at 1.5 A/cm^2 after only 100 cycles. Even though this is an accelerating tests due to the relatively slow H_2/air-front residence time and the high temperature, it is clear that these events have to be prevented or at least reduced by appropriate system strategies: i) designing for shorter residence times, since losses are directly proportional to residence time,[136] with $\approx$0.1 s being the practical minimum; ii) intermittant cell or stack shorting during start/stop (mostly described in the patent literature); and, iii) shutdown procedures which maintain small concentrations of H_2 in the anode compartment for as long as possible (many hours to many days) in order to minimize the number of unmitigated startups (again, only described in the patent literature).

From the material point of view, low-surface area graphitized carbon-supports offer substantial benefits with regards to durability at these conditions, but usually have lower BOL mass activities.[107] However, their start/stop degradation rates are up to 5-fold lower.[136] Other

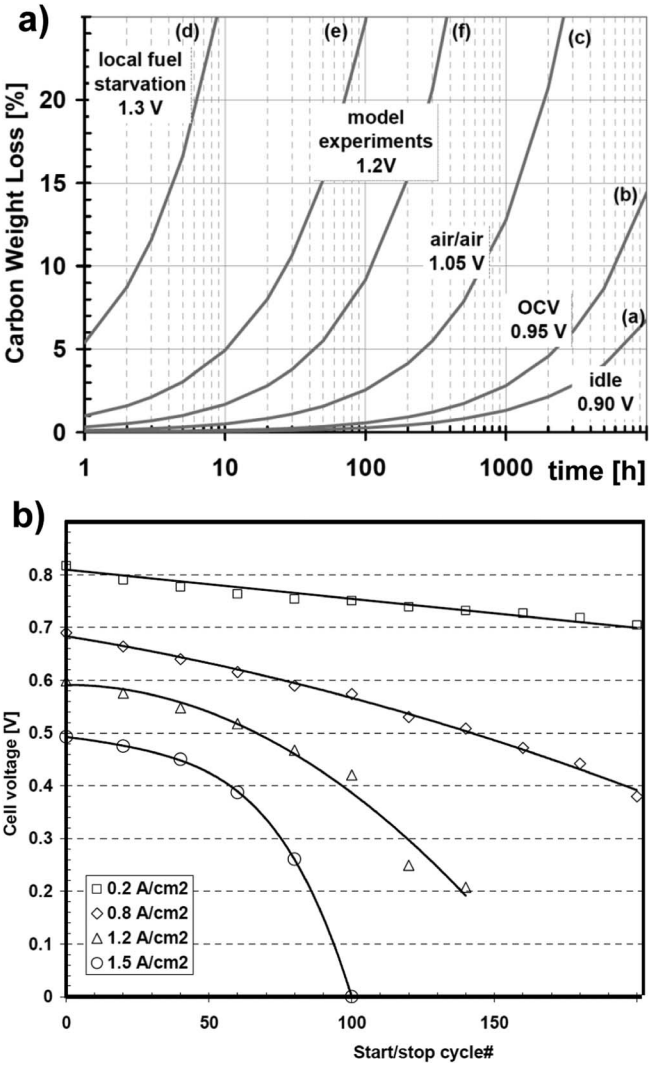

Figure 16. a) Estimated carbon weight loss versus time at 80°C and 100%RH, based on measured carbon corrosion kinetics: (a)–(e) for 50% Pt/C at different potentials, and, (f) for 30% Pt-alloy/corrosion-resistant carbon-support at 1.2 V. The potentials curves are defined to simulate the following operating conditions: (a) idle condition ($\approx$0.9 V), (b) OCV condition ($\approx$0.95 V), (c) air storage condition ($\approx$1.05 V), (d) local fuel starvation condition ($\approx$1.3 V), (e) and (f) model carbon corrosion experiments (typically at 1.2 V. b) Cell voltage decays at different current densities as a function of the number of start/stop cycles for a conventional carbon MEA at 80°C/66% RH with a H_2/air-front residence time of 1.3 s. (a) is reproduced from Makharia et al.,[125] and b) from Yu et al.[136] with permission from The Electrochemical Society.

materials approaches to lower cathode potentials during start/stop transients and hence degradation would be anode catalysts with improved selectivity for the HOR (i.e., having low ORR activity); so far, no suitable selective catalysts are available, but a similar effect can be achieved by reducing the platinum loading on the anode (possible because of the above discussed extremely high HOR activity of Pt). Similarly, catalysts with high oxygen evolution activity could mitigate high anodic potentials.[137] In the case of local fuel starvation, essentially a "H_2/air-front" produced by the permeation of oxygen through the membrane, can also be mitigated by membranes with lower oxygen permeation.[137] Next to the carbon loss during start/stop, significant loss of ECSA can be observed due to the large voltage-cycles occurring during start/stop events.[138] Topalov et.al. investigated voltage-cycling induced Pt dissolution and concluded, based on dissolution rates for polycrystalline Pt, that voltage excursions to above 1.1 V should be avoided.[139]

The future challenge for ORR catalyst development is to combine high mass activity catalyst concepts with more stable low-surface area graphitized carbon-supports. Alternative support materials have also been considered such as carbon nanotubes,[135] hollow graphitic spheres,[140] and conductive metal oxides.[141] Recently, Inaba et al. published MEA measurements with SiO_2 nanofiber supported Pt,[142] showing reasonable performance at intermediate humidification and poor performance under other commonly employed operating conditions. So far, none of these alternative supports seem to have the maturity to be used in commercial MEAs, and cumbersome and costly system mitigation strategies are still needed to assure long-term durability.

Transport losses at high local current densities.— To reach 0.1 g_{Pt}/kW, low MEA Pt loadings (≈0.05–0.10 mg_{Pt}/cm^2) and high current densities are mandatory as discussed before. This in turn means that high local current densities (i.e., high values of A/cm^2_{Pt}) are required. Unfortunately, under these conditions, mass-transport related voltage losses are observed for the cathode electrode, which currently cannot be clearly assigned, but which limit MEA performance at low cathode platinum loadings. Publications on this matter are available from Toyota, Nissan, and General Motors, all showing unassigned performance losses at low areal loadings, i.e., at low cathode roughness factors (roughness factor, rf, being defined as the Pt surface area per geometric MEA surface area, i.e., in units of $cm^2_{Pt}/cm^2_{cathode}$).[143,144,145] These losses might become even more important over the automotive life span, as the electrochemical surface area will further decrease due to ECSA losses (see above) and thus lead to even lower roughness factors. Consequently, increased voltages losses ascribed to unassigned mass transfer resistances after voltage-cycling induced ECSA losses have been reported.[146,147]

The appearance of cell voltage losses at low Pt loadings is illustrated in Figure 17, taken from a study by Owejan et al.[145] Based on simple Tafel kinetics for the ORR,[83] one would expect a parallel down-shift of the H_2/air polarization curves with decreasing Pt roughness factor, namely by 70 mV for each 10-fold decrease in roughness factor ($\Delta E_{kinetic} = 70\ mV \cdot \log[rf_1/rf_2]$, assuming a Tafel slope of 70 mV); since the Pt dispersion for the different catalysts used in this study is reasonably constant (≈60 m^2/g_{Pt}), the expected kinetic voltage loss between the highest Pt loading of 0.2 mg_{Pt}/cm^2 and the lowest loading of 0.025 mg_{Pt}/cm^2 would amount to $\Delta E_{kinetic} \approx 70\ mV \cdot \log(0.2/0.025) \approx 63$ mV, much larger than the actually observed losses in Fig. 17a. More insight can be gained by correcting the cell voltage by all the known and measurable voltage loss terms, viz., the bulk O_2 diffusion resistance through the GDL, the ohmic resistance due to proton transport through the membrane and electronic contact resistances, the proton transport resistance in the electrodes, and the hydrogen cross-over through the membrane. Assuming that simple Tafel kinetics hold, all the performance curves after these corrections should merge into one line when plotted versus the surface normalized current density (in units of A/cm^2_{Pt}). As can be seen in Figure 17b, this is the case up to ≈10 mA/cm^2_{Pt} or ≈0.70 V, but at higher current densities, a sharp downturn of the curves indicates the presence of yet unassigned voltage losses. The authors have modelled these losses by assuming interfacial resistances for oxygen transport through the gas/ionomer and the ionomer/Pt interface, even though the fundamental processes leading to these resistances are unclear.

Without considering these interfacial resistances, the oxygen permeability of the ionomer film which is thought to cover each Pt nanoparticle (≈5 nm thick if equally distributed) would need to be ≈10-fold lower than the value measured for thick ionomeric membranes (≈20 μm). Weber and Kusoglu reviewed the literature with regards to unassigned mass transfer losses and pointed out that there is experimental evidence for confinement effects with thin ionomer surface films, claimed to impact water uptake and oxygen permeability, so that the bulk ionomer properties may not reflect those of a nanometer thick surface film.[148] While similar observations were made in many studies,[149,150] the phenomenon is still not yet understood. Interestingly, the unassigned losses can be minimized for narrow flow-field land widths and for large channel/land ratios, which was explained by the more homogeneous current distribution under these conditions.[151] Similarly, in cell designs using a porous gas-distribution plate, the unassigned loss terms were almost undetectable.[152] In summary, the exact reasons for the unassigned loss remain ambiguous, but an understanding of its origin is of high importance for reaching the 0.1 g_{Pt}/kW target required for large-scale FCEV commercialization.

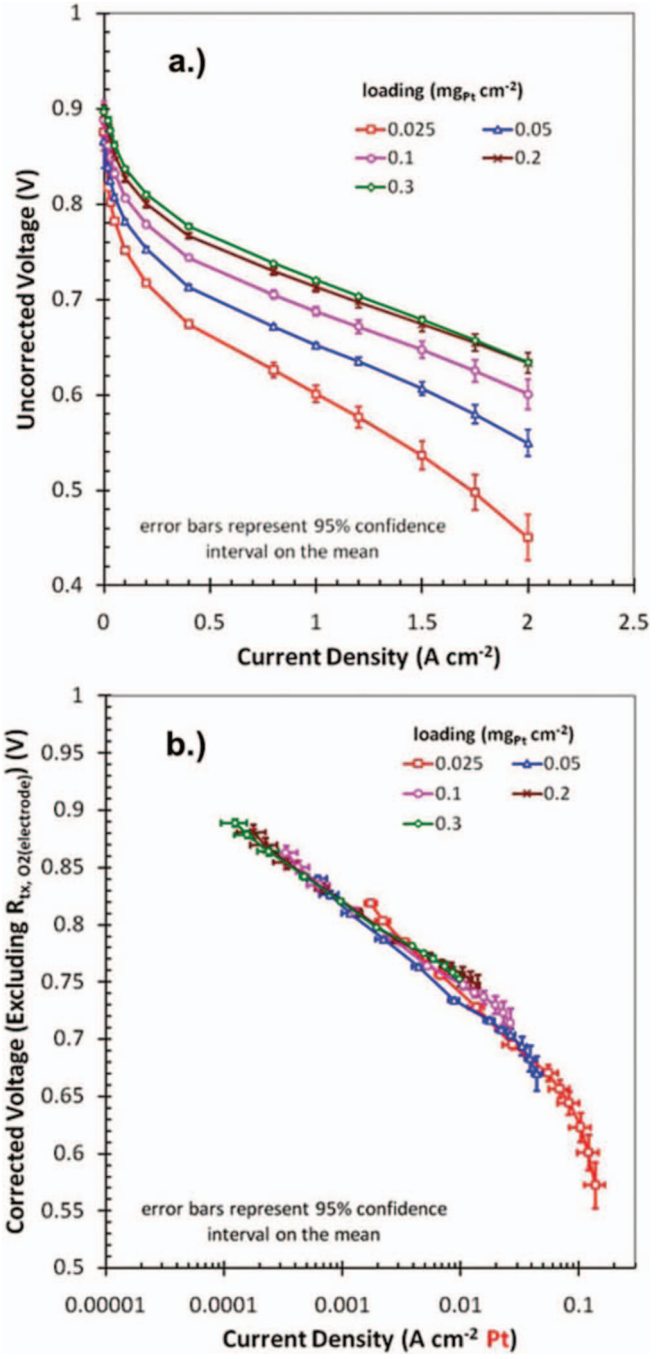

Figure 17. H_2/air performance (80°C, 100% relative humidity, H_2/air stoichiometry of 15/20 at 150 kPa_{abs}; 5 cm^2 single-cell) for different cathode platinum loadings, maintaining constant electrode thickness (≈11 μm) by varying the Pt wt% on a Vulcan carbon support (≈250 m^2/g BET). a) cell voltage vs. geometric current density; b) cell voltage corrected by the high-frequency resistance (HFR), electrode proton conduction resistance, bulk O_2 gas transport, and hydrogen cross-over vs. the Pt surface area normalized current density. (Reproduced from Owejan et al.[145] with permission from The Electrochemical Society.)

Membrane and ionomer performance & durability.— Over the last decade, significant advances have been made in the understanding of PFSA (perfluoro sulfonic acid) membrane durability, enabling the use of ultra-thin membranes in the range of 10–20 μm. These provide for very efficient water equilibration between anode and cathode as well as for low proton conduction resistances, which are key for high current density operation. Chemical and mechanical degradation have been investigated, and mitigation strategies for improved durability have been identified (see for example the comprehensive review by Gittleman et al.[153]). In brief, chemical degradation has been shown to be significantly decreased by the use of radical scavengers such as Ce^{3+} and Mn^{2+}. Also, end group stabilization, i.e., reducing the carboxylic group count by post-fluorination turned out to be effective against the so-called end-group unzipping mechanism.[154] While initially membranes were prone to mechanical degradation by relative humidity cycles,[81] improved membrane reinforcements were able to largely eliminate this issue.[155] Another mechanical issue is the shorting across membranes by diffusion media fibers, and improved GDL design can prevent fiber penetration. Also, the elimination of large particles, e.g., catalyst agglomerates or dust must be considered.

The technological advances in membrane/ionomer durability are accompanied by improvements in ionomer conductivity through the development of short side-chain ionomers which enable higher ion exchange capacities.[154] However, at lower relative humidity, desired for automotive stack operation,[81] a steep decline in proton conductivity is still observed. This leads to significant increase in performance loss due to increased resistance. This high relative humidity requirement still prevents high-temperature operation past the desired 100°C barrier. With regards to operation at low relative humidity, accelerated ionomer degradation under these conditions is still an issue, particularly at low platinum loadings, since the sulfate decomposition product significantly reduces the oxygen reduction kinetics of Pt.[156]

GDL performance.— For stack operation at high current densities, low effective diffusion length and high effective diffusion coefficients are important. Baker et al. showed that limiting current densities, i.e., effective diffusion coefficients, are dependent on the GDL thickness and that thinner GDLs in principle could enable higher current densities.[157] However, with decreasing GDL thickness, mass transport resistances across the flow-field land regions may become limiting, so that ideally the land width would have to be reduced. In addition, for thin GDLs their mechanical properties gain in importance: less stiff materials can decompress under wider channel geometries, leading to losses due to electrical contact resistances.[158] The recent trend toward finer flow-field features is reducing these losses.

The impact of liquid water saturation of GDLs on mass transport induced voltage losses, especially when stacks are operated at lower temperature and/or high current densities, critically affects the high current density performance. Experimental studies by Caulk and Baker[159] showed that the increased effective diffusion resistance under water-saturated conditions leads to approximately a doubling of the transport resistance, whereby the wet diffusion resistance was shown to depend on the thermal conductivity of the GDL. Quantifying liquid water saturation in GDLs is an important topic since it is required for rigorous performance modeling and for understanding the differences observed between hydrophobic and hydrophilic diffusion media.[160]

Finally, the GDL also affects the electrical contact resistance, which is a significant voltage loss term at high current densities[83] and reduced contact resistances particularly between the flow-field and the GDL would positively affect the g_{Pt}/kW figure-of-merit. In addition, that stiffer diffusion media cause more homogenous compression and thereby prevent damage to the catalyst layers during freeze-thaw cycles.[161] With regards to durability, it must be noted that the GDL's micro-porous layer underlies the same degradation mechanism as carbon based catalyst supports, so that it may gradually degrade at the high potential excursions during start/stop events,[162] which may become more noticeable as more corrosion resistant catalyst carbon-supports are employed.

Fuel cells for vehicle applications – summary.— Significant progress has been made over the last 10 years and concepts for platinum-based cathode catalysts with high mass activity catalysts have been developed, which are putting the targeted Pt loading reduction to the 10 g/FCEV in reach. The new class of Pt-alloy catalysts formed by dealloying also shows improved voltage-cycling stability, reaching the targets set by the DOE. The challenge for the FCEV generation to come is now to combine these catalyst concepts with support materials with higher durability in order to ensure fuel cell performance over FCEV service life. In addition, the origin of the yet unassigned mass transport losses at low Pt loadings must be understood and mitigated.

The main challenge in fuel cell membrane research seems to be to identify materials suited for higher operating temperatures and at low relative humidity in order to simplify system design, improve heat rejection, and reduce energy losses by the air compressor.

Conclusions

All-electric vehicles, either powered by batteries or by hydrogen fuel cells based on hydrogen produced from renewable energies seem to be the only viable option to meet the future CO_2 emission targets of <95 g_{CO2}/km. Which of these two technologies may succeed still depends on future research accomplishments, but we believe that some general conclusions can already be drawn with today's knowledge.

An analysis of the system-level energy density of lithium ion batteries (LiBs) suggests that the gravimetric energy density of advanced LiBs is unlikely to exceed 0.25 $kWh_{name\text{-}plate}/kg_{battery\text{-}system}$, which would limit the range of BEVs for the compact car market/pricing to ca. 200 miles, with recharging times substantially larger than that of conventional vehicles. Whether this will suffice for a large market penetration will depend not only on the *needed* but also on the *perceived* range requirement by customers. Higher energy densities would only be possible, if one were able to develop durable and safe metallic lithium anodes. While the so-called post-LiBs, viz., lithium-air and lithium-sulfur batteries have been assumed to revolutionize battery energy storage, cell- and system-level gravimetric energy densities are not expected to substantially exceed that of advanced LiBs; volumetric energy densities will most definitely be lower.

In contrast to BEVs, H_2-powered FCEVs are capable of large driving ranges (>300 miles) and can be refilled within several minutes. Besides the need for a hydrogen infrastructure based on hydrogen produced from renewable energy, a reduction of the platinum requirement per vehicle (currently ≈20–40 g_{Pt}/FCEV) still requires further development. Nevertheless, current data suggest that advanced catalysts (dealloyed Pt-alloys) are able to meet the long-term DOE activity and durability targets, but their integration into MEAs which can operate at high current densities and low Pt loadings still needs to be demonstrated.

Acknowledgments

The Section on lithium-sulfur batteries was written by O. G. from Volkswagen AG; the other Sections do not necessarily reflect the view of Volkswagen AG.

References

1. CO_2 Emissions from Fuel Combustion – Highlights, *International Energy Agency* (2014), http://www.iea.org/publications/freepublications/publication/CO2EmissionsFromFuelCombustionHighlights2014.pdf
2. Regulation (EU) No. 333/2014 of the European Parliament and of the Council of 11 March 2014, amending regulation (EC) No. 443/2009 to define the modalities for reaching the 2020 target to reduce CO_2 emissions from new passenger cars. Downloaded 08/15/2015, http://eur-lex.europa.eu/legal-content/EN/TXT/?uri=uriserv:OJ.L_.2014.103.01.0015.01.ENG.
3. U. Eberle, B. Müller, and R. von Helmolt, *Energy Environ. Sci.*, **5**, 8780 (2012).
4. O. Egbue and S. Long, *Energy Policy*, **48**, 717 (2012).
5. B. Dunn, H. Kamath, and J.-M. Tarascon, *Science*, **334**, 928 (2011).
6. B. R. Chalamala, T. Soundappan, G. R. Fisher, M. R. Anstey, V. V. Viswanathan, and M. L. Perry, *Proceedings of the IEEE*, **102**, 976 (2014).

7. K. E. Ayers, E. B. Anderson, K. T. Dreier, and K. W. Harrison, *ECS Transactions*, **50**(49), 35 (2013).
8. J. D. Holladay, J. Hu, D. L. King, and Y. Wang, *Catalysis Today*, **139**, 244 (2009).
9. BMW i3 technical data (accessed 08/16/2015), http://www.bmw.com/com/en/newvehicles/i/i3/2013/showroom/technical_data.html
10. F. T. Wagner, B. Lakshmanan, and M. F. Mathias, *J. Phys. Chem. Lett.*, **1**, 2204 (2010).
11. K. G. Gallagher, S. Goebel, T. Greszler, M. Mathias, W. Oelerich, D. Eroglu, and V. Srinivasan, *Energy Environ. Sci.*, **7**, 1555 (2014).
12. D. Andre, S.-J. Kim, P. Lamp, S. F. Lux, F. Maglia, O. Paschos, and B. Stiaszny, *J. Mater. Chem. A*, **3**, 6709 (2015).
13. D. Papageorgopoulos, "Fuel Cells Program – Plenary Presentation," presented at the 2015 DoE Annual Merit Review (accessed 08/16/2015), http://www.hydrogen.energy.gov/pdfs/review15/fc000_papageorgopoulos_2015_o.pdf
14. N. T. Stetson, "Hydrogen Storage Program Area – Plenary Presentation", presented at the 2015 DoE Annual Merit Review (accessed 08/16/2015), http://www.hydrogen.energy.gov/pdfs/review15/st000_stetson_2015_o.pdf
15. T. Franke and J. F. Krems, *Transport Policy*, **30**, 56 (2013).
16. J. O. Estima and A. J. M. Cardoso, *IEEE Transactions on Vehicular Technology*, **61**, 1021 (2012).
17. J. T. Lee, S. Kwon, Y. Lim, M. S. Chon, and D. Kim, *SAE Technical Paper*, 2013-01-0400 (2013).
18. 24 kW fast-charging stations from BMW (accessed 08/17/2015), http://www.bmwicharging.com/BMWiDCFastCharger.
19. 120 kW supercharger from Tesla (accessed 08/17/2015), http://www.teslamotors.com/supercharger.
20. A. Schroeder and T. Traber, *Energy Policy*, **43**, 136 (2012).
21. S. Sprik, J. Kurtz, C. Ainscough, and M. Peters, "Next Generation Hydrogen Station Composite Data Products – Data through Quarter 4 of 2014," *National Renewable Energy Laboratory*, USA (accessed 08/16/2015), http://www.nrel.gov/docs/fy15osti/64317.pdf.
22. A. Yamashita, M. Kondo, S. Goto, and N. Ogani, *SAE Technical Paper*, 2015-01-1169 (2015).
23. N. Rauh, T. Franke, and J. F. Krems, *Human Factors*, **57**, 177 (2015).
24. M. M. Thackeray, S.-H. Kang, C. S. Johnson, J. T. Vaughey, R. Benedek, and S. A. Hackney, *J. Mater. Chem.*, **17**, 3112 (2007).
25. F. Amalraj, M. Talianker, B. Markovsky, D. Sharon, L. Burlaka, F. Shafir, E. Zinigrad, O. Haik, D. Aurbach, J. Lampert, M. Schulz-Dobrick, and A. Garsuch, *J. Electrochem. Soc.*, **160**, A324 (2013).
26. E. Kramer, T. Schedlbauer, B. Hoffmann, L. Terborg, S. Nowak, H. J. Gores, S. Passerini, and M. Winter, *J. Electrochem. Soc.*, **160**, A356 (2013).
27. M. Metzger, C. Marino, J. Sicklinger, D. Haering, and H. A. Gasteiger, *J. Electrochem. Soc.*, **162**, A1123 (2015).
28. J. Heine, S. Krüger, C. Hartnig, U. Wietelmann, M. Winter, and P. Bieker, *Adv. Energy Mater.*, **4**, 1300815 (2014).
29. W. Xu, J. Wang, F. Ding, X. Chen, E. Nasybulin, Y. Zhang, and J.-G. Zhang, *Energy Environ. Sci.*, **7**, 513 (2014).
30. A. C. Luntz and B. D. McCloskey, *Chem. Rev.*, **114**, 11721 (2014).
31. Y.-C. Lu, H. A. Gasteiger, M. C. Parent, V. Chiloyan, and Y. Shao-Horn, *Electrochem. and Solid State Lett.*, **13**, A69 (2010).
32. K. M. Abraham and J. Jiang, *J. Electrochem. Soc.*, **143**, 1 (1996).
33. A. Débart, A. J. Paterson, J. Bao, and P. G. Bruce, *Angew. Chem. Int. Ed.*, **47**, 5421 (2008).
34. F. Mizuno, S. Nakanishi, Y. Kotani, S. Yokoishi, and H. Iba, *Electrochemistry*, **78**, 403 (2010).
35. S. A. Freunberger, Y. Chen, Z. Peng, J. M. Griffin, L. J. Hardwick, F. Bardé, P. Nová, and P. G. Bruce, *J. Am. Chem. Soc.*, **133**, 8040 (2011).
36. B. D. McCloskey, D. S. Bethune, R. M. Shelby, G. Girishkumar, and A. C. Luntz, *J. Phys. Chem. Lett.*, **2**, 1161 (2011).
37. B. D. McCloskey, D. S. Bethune, R. M. Shelby, T. Mori, R. Scheffler, A. Speidel, M. Sherwood, and A. C. Luntz, *J. Phys. Chem. Lett.*, **3**, 3043 (2012).
38. N. Tsiouvaras, S. Meini, I. Buchberger, and H. A. Gasteiger, *J. Electrochem. Soc.*, **160**, A471 (2013).
39. R. Black, S. H. Oh, J.-H. Lee, T. Yim, B. Adams, and L. F. Nazar, *J. Am. Chem. Soc.*, **134**, 2902 (2012).
40. K. U. Schwenke, S. Meini, X. Wu, H. A. Gasteiger, and M. Piana, *Phys. Chem. Chem. Phys.*, **15**, 11830 (2013).
41. V. S. Bryantssev, J. Uddin, V. Giordani, W. Walker, D. Addison, and G. V. Chase, *J. Electrochem. Soc.*, **160**, A160 (2013).
42. V. S. Bryantsev and F. Faglioni, *J. Phys. Chem. A*, **116**, 7128 (2012).
43. W. Walker, V. Giordani, J. Uddin, V. S. Bryantsev, G. V. Chase, and D. Addison, *J. Am. Chem. Soc.*, **135**, 2076 (2013).
44. B. D. Adams, R. Black, Z. Williams, R. Fernandes, M. Cuisinier, E. J. Berg, P. Novak, G. K. Murphy, and L. F. Nazar, *Adv. Energy Mater.*, **5**, 1400867 (2015).
45. G. A. Elia, J. Hassoun, W.-J. Kwak, Y.-K. Sun, B. Scrosati, F. Mueller, D. Bresser, S. Passerini, P. Oberhumer, N. Tsiouvaras, and J. Reiter, *Nano Lett.*, **14**, 6572 (2014).
46. K U. Schwenke, J. Herranz, H. A. Gasteiger, and M. Piana, *J. Electrochem. Soc.*, **162**, A905 (2015).
47. B. M. Gallant, R. R. Mitchell, D. G. Kwabi, J. Zhou, L. Zuin, C. V. Thompson, and Y. Shao-Horn, *J. Phys. Chem. C*, **116**, 20800 (2012).
48. M. M. O. Thotiyl, S. A. Freunberger, Z. Peng, and P. G. Bruce, *J. Am. Chem. Soc.*, **135**, 494 (2013).
49. B. D. McCloskey, A. Speidel, R. Scheffler, D. C. Miller, V. Viswanathan, J. S. Hummelshøj, J. K. Nørskov, and A. C. Luntz, *J. Phys. Chem. Lett.*, **3**, 997 (2012).
50. S. Meini, N. Tsiouvaras, K. U. Schwenke, M. Piana, H. Beyer, L. Lange, and H. A. Gasteiger, *Phys. Chem. Chem. Phys.*, **15**, 11478 (2013).
51. M. M. O. Thotiyl, S. A. Freunberger, Z. Peng, Y. Chen, Z. Liu, and P. G. Bruce, *Nature Materials*, **12**, 1050 (2013).
52. S. Meini, M. Piana, N. Tsiouvaras, A. Garsuch, and H. A. Gasteiger, *Electrochem. and Solid-State Lett.*, **15**, A45 (2012).
53. V. Viswanathan, K. S. Thygesen, J. S. Hummelshøj, J. K. Nørskov, G. Girishkumar, B. D. McCloskey, and A. C. Luntz, *J. Chem. Phys.*, **135**, 214704 (2011).
54. S. Meini, M. Piana, H. Beyer, J. Schwämmlein, and H. A. Gasteiger, *J. Electrochem. Soc.*, **159**, A2135 (2012).
55. K. U. Schwenke, M. Metzger, T. Restle, M. Piana, and H. A. Gasteiger, *J. Electrochem. Soc.*, **162**, A573 (2015).
56. N. B. Aetukuri, B. D. McCloskey, J. M. Garcia, L. E. Krupp, V. Viswanathan, and A. C. Luntz, *Nature Chemistry*, **7**, 50 (2015).
57. B. D. McCloskey, R. Scheffler, A. Speidel, D. S. Bethune, R. M. Shelby, and A. C. Luntz, *J. Am. Chem. Soc.*, **133**, 18038 (2011).
58. G. Chase, S. Zecevic, T. W. Walker, J. Uddin, K. A. Sasaki, P. V. Giordani, V. Bryantsev, M. Blanco, D. D. Addison, and US Application, filed April 25, 2011, published Feb. 2, 2012.
59. M. Agostini, Y. Aihara, T. Yamada, B. Scrosati, and J. Hassoun, *Solid State Ionics*, **244**, 48 (2013).
60. M. Nagao, A. Hayashi, and M. Tatsumisago, *Electrochim. Acta*, **56**, 6055 (2011).
61. Y. Zhao, Y. Zhang, D. Gosselink, T. N. L. Doan, M. Sadhu, H.-J. Cheang, and P. Chen, *Membranes*, **2**, 553 (2012).
62. J. Kim, D.-J. Lee, H.-G. Jung, Y.-K. Sun, J. Hassoun, and B. Scrosati, *Adv. Funct. Mater.*, **23**, 1076 (2013).
63. G. He, S. Evers, X. Liang, M. Cuisinier, A. Garsuch, and L. F. Nazar, *ACS Nano*, **7**, 10920 (2013).
64. Z. Sun, M. Xiao, S. Wang, D. Han, S. Song, G. Chen, and Y. Meng, *J. Power Sources*, **285**, 478 (2015).
65. N. Jayaprakash, J. Shen, S. S. Moganty, A. Corona, and L. A. Archer, *Angew. Chem.*, **123**, 6026 (2011).
66. D. Aurbach, E. Pollak, R. Elazari, G. Salitra, C. S. Kelley, and John Affinito, *J. Electrochem. Soc.*, **156**, A694 (2009).
67. S. Dalavi, P. Guduru, and B. L. Lucht, *J. Electrochem. Soc.*, **159**, A642 (2012).
68. J. Hassoun and B. Scrosati, *Angew. Chem.*, **122**, 2421 (2010).
69. D. Eroglu, K. R. Zavadil, and K. G. Gallagher, *J. Electrochem. Soc.*, **162**, A982 (2015).
70. M. Hagen, D. Hanselmann, K. Ahlbrecht, R. Maça, D. Gerber, and J. Tübke, *Adv. Energy Mater.*, **5**, 1401986 (2015).
71. J. Brückner, S. Thieme, F. Böttger-Hiller, I. Bauer, H. T. Grossmann, P. Strubel, H. Althues, S. Spange, and S. Kaskel, *Adv. Funct. Mater.*, **24**, 1284 (2014).
72. From Sion Power website (accessed 08/26/2105), http://www.sionpower.com/product.html.
73. R. M. Busche, P. Adelhelm, H. Sommer, H. Schneider, K. Leitner, and J. Janek, *J. Power Sources*, **259**, 289 (2014).
74. D. Aurbach, E. Zinigrad, Y. Cohen, and H. Teller, *Solid State Ionics*, **148**, 405 (2002).
75. H. Jha, I. Buchberger, X. Cui, S. Meini, and H. A. Gasteiger, *J. Electrochem. Soc.*, **162**, A1829 (2015).
76. Roland Berger Strategy Consultants (presented October 2012), http://www.rolandberger.de/media/pdf/Roland_Berger_Li_Ion_Batteries_Bubble_Bursts_20121019.pdf.
77. From Oxis website (accessed 08/26/2015), http://www.oxisenergy.com/technology/.
78. B. D. James and A. B. Spisak, "Mass Production Cost Estimation of Direct H_2 PEM Fuel Cell Systems for Transportation Applications: 2012 Update", DOE Award Number DE-EE0005236, http://www1.eere.energy.gov/hydrogenandfuelcells/pdfs/sa_fc_system_cost_analysis_2012.pdf (accessed 08/30/2015).
79. Y. Wang, K. S. Chen, J. Mishler, S. C. Cho, and X. C. Adroher, *Appl. Energy*, **88**, 981 (2011).
80. Fuel Cell Technical Team Road Map (online 2013; accessed 08/15/2015), http://energy.gov/sites/prod/files/2014/02/f8/fctt_roadmap_june2013.pdf.
81. M. F. Mathias, R. Makharia, H. A. Gasteiger, J. J. Conley, T. J. Fuller, C. J. Gittleman, S. S. Kocha, D. P. Miller, C. K. Mittelsteadt, T. Xie, S. G. Yan, and P. T. Yu., *The Electrochemical Society Interface*, **14** (Fall issue), 24 (2005).
82. W. Bernhart, S. Riederle, and M. Yoon, "Fuel Cells – A realistic alternative for zero emission?", *Roland Berger Strategy Consultants* (online 2014; accessed 08/15/2015), http://www.rolandberger.de/media/pdf/Roland_Berger_Fuel_cells_20140113.pdf.
83. W. Gu, D. R. Baker, Y. Liu, and H. A. Gasteiger, in *Handbook of Fuel Cells - Fundamentals, Technology and Applications*, eds. H. Yokokawa, H. A. Gasteiger, and W. Vielstich, John Wiley & Sons, Chichester, vol. **6**, 631 (2009).
84. Y Wang, G. Wang, G. Li, B. Huang, J. Pan, Q. Liu, J. Han, L. Xiao, J. Lu, and L. Zhuang, *Energy Environ. Sci.*, **8**, 177 (2015).
85. N. Konno, S. Mizuno, H. Nakaji, and Y. Ishikawa, *SAE International Journal of Alternative Powertrains*, **4**, 123 (2015).
86. K. Shinozaki, H. Yamada, and Y. Morimoto, *J. Electrochem. Soc.*, **158**, B467 (2011).
87. N. Nakagaki, *SAE Technical Paper*, 2015-01-1174 (2015).
88. A. Ohma, K. Shinohara, A. Iiyama, T. Yoshida, and A. Daimaru, *ECS Trans.*, **41**(1), 775, (2011).
89. K. C. Neyerlin, W. Gu, J. Jorne, and H. A. Gasteiger, *J. Electrochem. Soc.*, **154**, B631 (2007).
90. A. Rabis, P. Rodriguez, and T. J. Schmidt, *ACS Catalysis*, **2**, 864 (2012).

91. J. Zhang, in *Fuel Cells: Selected Entries from the Encyclopedia of Sustainability Science and Technology*, ed. K. D. Kreuer, Springer Science + Business Media, New York, p. 305 (2013).
92. A. J. Appleby, in *Comprehensive Treatise of Electrochemistry*, eds. J. O. M. Bockris, E. Yeager, S. U. M. Khan, R. E. White, and B. E. Conway, Plenum Press, New York, Vol. **7**, p. 173 (1983).
93. J. K. Nørskov, J. Rossmeisl, A. Logadottir, L. Lindqvist, J. R. Kitchin, T. Bligaard, and H. Jónsson, *J. Phys. Chem. B.*, **108**, 17886 (2004).
94. H. A. Gasteiger, S. S. Kocha, B. Sompalli, and F. T. Wagner, *Appl. Catal. B: Env.*, **56**, 9 (2005).
95. G. A. Tritsaris, J. Greeley, J. Rossmeisl, and J. K. Nørskov, *Catal. Lett.*, **141**, 909 (2011).
96. U. A. Paulus, A. Wokaun, G. G. Scherer, T. J. Schmidt, V. Stamenkovic, N. M. Markovic, and P. N. Ross, *Electrochim. Acta*, **47**, 3787 (2002).
97. D. Thompsett, in *Handbook of Fuel Cells - Fundamentals, Technology and Applications*, eds. A. Lamm, H. A. Gasteiger, and W. Vielstich, John Wiley & Sons, Chichester, vol. **3**, 467 (2003).
98. P. Hernandez-Fernandez, F. Masini, D. N. McCarthy, C. E. Strebel, D. Friebel, D. Deiana, P. Malacrida, A. Nierhoff, A. Bodini, A. M. Wise, J. H. Nielsen, T. W. Hansen, A. Nilsson, I. E. L. Stephens, and I. Chorkendorff, *Nature Chemistry*, **6**, 732 (2014).
99. V. M. Jalan and E. J. Taylor, *J. Electrochem. Soc.*, **130**, 2299 (1983).
100. J. Zhang, M. B. Vukmirovic, Y. Xu, M. Mavrikakis, and R. R. Adzic, *Angew. Chem.*, **117**, 2170 (2005).
101. V. R. Stamenkovic, B. S. Mun, K. J. J. Mayrhofer, P. N. Ross, and N. M. Markovic, *J. Am. Chem. Soc.*, **128**, 8813 (2006).
102. V. R. Stamenkovic, B. S. Mun, K. J. J. Mayrhofer, P. N. Ross, N. M. Markovic, J. Rossmeisl, J. Greeley, and J. K. Nørskov, *Angew. Chem. Int. Ed.*, **45**, 2897 (2006).
103. M. L. B. Rao, A. Damjanovic, and J. O. M. Bockris, *J. Phys. Chem.*, **67**, 2508 (1963).
104. B. Hammer and J. K. Nørskov, *Advances in Catalysis*, **45**, 71 (2000).
105. V. R. Stamenkovic, B. Fowler, B. S. Mun, G. Wang, P. N. Ross, C. A. Lucas, and N. M. Markovic, *Science*, **315**, 493 (2007).
106. S. Chen, P. J. Ferreira, W. Sheng, N. Yabuuchi, L. F. Allard, and Y. Shao-Horn, *J. Am. Chem. Soc.*, **130**, 13818 (2008).
107. F. T. Wagner, S. G. Yan, and P. T. Yu, *Handbook of Fuel Cells - Fundamentals, Technology and Applications*, eds. H. Yokokawa, H. A. Gasteiger, and W. Vielstich, John Wiley & Sons, Chichester, vol. **5**, 250 (2009).
108. P. Strasser, *Rev. Chem. Eng.*, **25**, 255 (2009).
109. S. Koh, N. Hahn, C. Yu, and P. Strasser, *J. Electrochem. Soc.*, **155**, B1281 (2008).
110. Z. Yu, J. Zhang, Z. Liu, J. M. Ziegelbauer, H. Xin, I. Dutta, D. A. Muller, and F. T. Wagner, *J. Phys. Chem. C*, **116**, 19877 (2012).
111. M. Oezaslan, F. Hasché, and P. Strasser, *J. Electrochem. Soc.*, **159**, B25 (2012).
112. L. Gan, M. Heggen, R. O'Malley, B. Theobald, and P. Strasser, *Nano Lett.*, **13**, 1131 (2013).
113. B. Han, C. E. Carlton, A. Kongkanand, R. S. Kukreja, B. R. Theobald, L. Gan, R. O'Malley, P. Strasser, F. T. Wagner, and Y. Shao-Horn, *Energy Environ. Sci.*, **8**, 258 (2015).
114. M. K. Debe, *ECS Trans.*, **45**, 47 (2012).
115. J. Zhang, F. H. B. Lima, M. H. Shao, K. Sasaki, J. X. Wang, J. Hanson, and R. R. Adzic, *J. Phys. Chem. B*, **109**, 22701 (2005).
116. S. Ball, S. L. Burton, J. Fisher, R. O'Malley, B. Tessier, B. R. C. Theobald, D. Thompsett, W. P. Zhou, D. Su, Y. Zhu, and R. R. Adzic, *ECS Trans.*, **25**, 1023 (2009).
117. Y. J. Wang, N. Zhao, B. Fang, H. Li, Y. T. Bi, and H. Wang, *Chem. Rev.*, **115**, 3433 (2015).
118. M. K. Carpenter, T. E. Moylan, R. S. Kukreja, M. H. Atwan, and M. M. Tessema, *J. Am. Chem. Soc.*, **134**, 8535 (2012).
119. C. Cui, L. Gan, M. Heggen, S. Rudi, and P. Strasser, *Nature Materials*, **12**, 765 (2013).
120. H. A. Gasteiger and N. M. Markovic, *Science*, **324**, 48 (2009).
121. C. Chen, Y. Kang, Z. Huo, Z. Zhu, W. Huang, H. L. Xin, J. D. Snyder, D. Li, J. A. Herron, M. Mavrikakis, M. Chi, K. L. More, Y. Li, N. M. Markovic, G. A. Somorjai, P. Yang, and V. R. Stamenkovic, *Science*, **343**, 1339 (2014).
122. A. Ishihara, Y. Ohgi, K. Matsuzawa, S. Mitsushima, and K.-I Ota, *Electrochim. Acta*, **55**, 8005 (2010).
123. E. Proietti, F. Jaouen, M. Lefèvre, N. Larouche, J. Tian, J. Herranz, and J.-P. Dodelet, *Nature Communications*, **2**, article# 416 (2011).
124. G. Wu, K. L. More, C. M. Johnston, and P. Zelenay, *Science*, **332**, 443 (2011).
125. R. Makharia, S. S. Kocha, P. T. Yu, M. A. Sweikart, W. Gu, F. T. Wagner, and H. A. Gasteiger, *ECS Trans.*, **1**(8), 3 (2006).
126. C. A. Reiser, L. Bregoli, T. W. Patterson, J. S. Yi, J. D. L. Yang, M. L. Perry, and T. D. Jarvi, *Electrochem. Solid-State Lett.*, **8**, A273 (2005).
127. T. W. Patterson and R. M. Darling, *Electrochem. Solid-State Lett.*, **9**, A183 (2006).
128. A. Taniguchi, T. Akita, K. Yasuda, and Y. Miyazaki, *J. Power Sources*, **130**, 42 (2004).
129. a). P. J. Ferreira, G. J. la O', Y Shao-Horn, D. Morgan, R. Makharia, S. Kocha, and H. A. Gasteiger, *J. Electrochem. Soc.*, **152**, A2256 (2005); b). Y. Shao-Horn, W. C. Sheng, S. Chen, P. J. Ferreira, E. F. Holby, and D. Morgan, *Top. Catal.*, **46**, 285 (2007).
130. S. S. Kocha, in *Polymer Electrolyte Fuel Cell Degradation*, eds. E. C. Kumbur, T. N. Veziroglu, and M. M. Mench, Elsevier Inc., Waltham (2012).
131. S. Chen, H. A. Gasteiger, K. Hayakawa, T. Tada, and Y. Shao-Horn, *J. Electrochem. Soc.*, **157**, A82 (2010).
132. T. A. Greszler, T. E. Moylan, and H. A. Gasteiger, in *Handbook of Fuel Cells - Fundamentals, Technology and Applications*, eds. H. Yokokawa, H. A. Gasteiger, and W. Vielstich, John Wiley & Sons, Chichester, Vol. **6**, p. 728 (2009).
133. J. Zhang, K. Sasaki, E. Sutter, and R. R. Adzic, *Science*, **315**, 220 (2006).
134. H. Matsumori, S. Takenaka, H. Matsun, and M. Kishida, *ECS Trans.*, **25**, 689 (2009).
135. N. C. Cheng, M. N. Banis, J. Liu, A. Riese, X. Li, R. Y. Li, S. Y. Ye, S. Knights, and X. L. Sun, *Adv. Mater.*, **27**, 277 (2015).
136. P. T. Yu, W. Gu, R. Makharia, F. T. Wagner, and H. A. Gasteiger, *ECS Trans.*, **3**(1), 797 (2006).
137. W. Gu, P. T. Yu, R. N. Carter, R. Makharia, and H. A. Gasteiger, in *Modeling and Diagnostics of Polymer Electrolyte Fuel Cells, Modern Aspects of Electrochemistry*, eds. C.-Y. Wang and U. Pasaogullari, Springer Science+Business Media, Vol. 49, 45 (2010).
138. H. Schulenburg, B. Schwanitz, J. Krbanjevic, N. Linse, G. G. Scherer, and A. Wokaun, *Electrochem. Comm.*, **13**, 921 (2011).
139. A. A. Topalov, I. Katsounaros, M. Auinger, S. Cherevko, J. C. Meier, S. O. Klemm, and K. J. J. Mayrhofer, *Angew. Chem. Int. Ed.*, **51**, 12613 (2012).
140. C. Galeano, J. C. Meier, V. Peinecke, H. Bongard, I. Katsounaros, A. A. Topalov, A. Lu, K. J. J. Mayrhofer, and F. Schüth, *J. Am. Chem. Soc.*, **134**, 20457 (2012).
141. T. Tsukatsune, Y. Takabatake, Z. Noda, T. Daio, A. Zaitsu, and S. M. Lyth., *J. Electrochem. Soc.*, **161**, F1208 (2014).
142. M. Inaba, T. Suzuki, T. Hatanaka, and Y. Morimoto, *J. Electrochem. Soc.*, **162**, F634 (2015).
143. N. Nonoyama, S. Okazaki, A. Z. Weber, Y. Ikogi, and T. Yoshida., *J. Electrochem. Soc.*, **158**, B416 (2011).
144. K. Sakai, K. Sato, T. Mashio, A. Ohma, K. Yamaguchi, and K. Shinohara, *ECS Trans.*, **25**, 1193 (2009).
145. J. P Owejan, J. E. Owejan, and W. Gu, *J. Electrochem. Soc.*, **160**, F824 (2013).
146. S. Jomori, N. Nonoyama, and T. Yoshida, *J. Power Sources*, **215**, 18 (2012).
147. T. A. Greszler, D. Caulk, and P. Sinha., *J. Electrochem. Soc.*, **159**, F831 (2012).
148. A. Z. Weber and A. Kusoglu, *J. Mater. Chem. A*, **2**, 17207 (2014).
149. Y. Ono, A. Ohma, K. Shinohara, and K. Fushinobu, *J. Electrochem. Soc.*, **160**, F779.
150. T. Suzuki, K. Kudo, and Y. Morimoto, *J. Power Sources*, **222**, 379 (2013).
151. Y. Fukuyama, T. Shiomi, T. Kotaka, and Y. Tabuchi, *Electrochim. Acta*, **117**, 367 (2014).
152. A. K. Srouji, L. J. Zheng, R. Dross, and M. M. Mench, *ECS Trans.*, **58**, 807 (2013).
153. C. S. Gittleman, F. D. Coms, and Y.-H. Lai, in *Polymer Electrolyte Fuel Cell Degradation*, eds. E. C. Kumbur, T. N. Veziroglu, and M. M. Mench, Elsevier Inc., Waltham, p. 15 (2012).
154. L. Merlo, A. Ghielmi, and V. Arcella, in *Encyclopedia of Electrochemical Power Sources*, eds. C. Dyer, P. Moseley, Z. Ogumi, D. Rand, B. Scrosati, and J. Garche, Elsevier, Amsterdam, p. 680 (2009).
155. W. K. Liu, S. J. C. Cleghorn, B. E. Delaney, and M. Crum, *Handbook of Fuel Cells - Fundamentals, Technology and Applications*, eds. H. Yokokawa, H. A. Gasteiger, and W. Vielstich, John Wiley & Sons, Chichester, Vol. **5**, p. 385 (2009).
156. J. Zhang, J. B. A. Litteer, F. D. Coms, and R. Makharia, *J. Electrochem. Soc.*, **159**, F287 (2012).
157. D. R. Baker, D. A. Caulk, K. C. Neyerlin, and M. W. Murphy, *J. Electrochem. Soc.*, **156**, B991 (2009).
158. J. Kleemann, F. Finsterwalder, and W. Tillmetz, *J. Power Sources*, **190**, 92 (2009).
159. D. A. Caulk and D. R. Baker, *J. Electrochem. Soc.*, **157**, B1237 (2010).
160. T. Tanuma and S. Kinoshita, *J. Electrochem. Soc.*, **161**, F94 (2014).
161. S. Kim, B. K. Ahn, and M. M. Mench, *J. Power Sources*, **179**, 140 (2008).
162. M. L. Perry, T. Patterson, and T. Madden, *ECS Trans.*, **33**, 1081 (2010).

Journal of The Electrochemical Society, **163** (7) X3-X3 (2016)
0013-4651/2016/163(7)/X3/1/$33.00 © The Electrochemical Society

Erratum: Review—Electromobility: Batteries or Fuel Cells? [*J. Electrochem. Soc.*, 162, A2605 (2015)]

Oliver Gröger,[a] Hubert A. Gasteiger,[b] and Jens-Peter Suchsland[c]

[a] *Volkswagen AG, 38436 Wolfsburg, Germany*
[b] *Chair of Technical Electrochemistry, Technische Universität München, 85748 Garching, Germany*
[c] *SolviCore GmbH & Co. KG, 63457 Hanau, Germany*

On page A2610, left column, the first sentence after the subheading *Lithium-sulfur battery concept.*— should be

Due to the high specific energy of the sulfur cathode (1675 mAh/g_S), lithium-sulfur batteries have also been considered as promising post-LiB technology with substantial gravimetric energy density and cost advantages over LiBs.

On pages A2610, right column, first paragraph, the sentence that continues onto page A2611 and remainder of the paragraph should be

The third strategy is to use silicon based anodes instead of metallic lithium anodes (see Fig. 6c), with the hope that a more stable SEI on silicon compared to metallic lithium might prevent/suppress several detrimental processes: i) the polysulfide redox-shuttle; ii) the continuous consumption of sulfur via polysulfide reduction and Li_2S precipitation at the anode; and, iii) the long-term consumption of SEI stabilizing additives like $LiNO_3$.[66] Other additives which are effective for silicon anodes (e.g., vinylene carbonate[67]) are typically dissolved in carbonate electrolytes. These carbonate electrolytes are shown to be incompatible with polysulfides.[163] Another possible anode alternative might be tin-based electrodes as shown by Scrosati et al.[68]

On page 2614, left column, third paragraph, the first sentence should be

Assuming that the cost breakdown of a battery cell with a metallic lithium anode is similar to that of a battery cell with a graphite anode, and considering that the price of sulfur is negligible compared to NMC111, one would project a cost advantage of about 23% for a Li/Li_2S (or Li/S) battery cell.

On page A2622, Reference 163 should be

163. T. Yim, M. Park, J. Yu, K. Kim, K. Im, J. Kim, G. Jeong, Y. Jo, S. Woo, K. Kang, 37 I. Lee, and Y. Kim, *Electrochem. Acta*, **107**, 454 (2013).